DSPACE

https://dspace.org/

# Polymer Template Selection for 1D Metal Oxide Gas Sensors A Review

**Khanyisile Nkuna; Teboho Clement Mokhena; Rudolph Erasmus; Katekani Shingange**

https://hdl.handle.net/10539/47123
WOS

Downloaded from a DSpace repository. https://dspace.org/

processes

MDPI

*Review*

# Polymer Template Selection for 1D Metal Oxide Gas Sensors: A Review

**Khanyisile Sheryl Nkuna [1], Teboho Clement Mokhena [2,3,*], Rudolph Erasmus [1] and Katekani Shingange [1,*]**

[1] Materials Physics Research Institute (MPRI), School of Physics, University of the Witwatersrand, Private Bag 3, Johannesburg 2050, South Africa; 2318077@students.wits.ac.za (K.S.N.); rudolph.erasmus@wits.ac.za (R.E.)
[2] DSTI/Mintek Nanotechnology Innovation Centre (NIC), Advanced Materials Division, Mintek, 200 Malibongwe Drive, Private Bag X3015, Randburg 2125, South Africa
[3] School of Chemical and Physical Sciences, University of Mpumalanga, Mbombela 1200, South Africa
* Correspondence: tebohom@mintek.co.za (T.C.M.); katekani.shingange@wits.ac.za (K.S.)

**Abstract**

The increasing demand for reliable, sensitive, and cost-effective gas sensors drives ongoing research in this field. Ideal gas sensors must demonstrate high sensitivity and selectivity, stability, rapid response and recovery times, energy efficiency, and affordability. One-dimensional (1D) metal oxide semiconductors (MOSs) are prominent candidates due to their excellent sensing properties and straightforward fabrication processes. The sensing efficacy of 1D MOSs is heavily dependent on their surface area and porosity, which influence gas interaction and detection efficiency. Polymeric templates serve as effective tools for enhancing these properties by enabling the creation of uniform, porous nanostructures with high surface area, thereby improving gas adsorption, sensitivity, and dynamic response characteristics. This review systematically examines the role of polymeric templates in the construction of 1D MOSs for gas sensing applications. It discusses critical factors influencing polymer template selection and how this choice affects key microstructural parameters, such as grain size, pore distribution, and defect density, essential to sensor performance. The recent literature highlights the mechanisms through which polymer templates facilitate the fine-tuning of nanostructures. Future research directions include exploring novel polymer architectures, developing scalable synthesis methods, and integrating these sensors with emerging technologies.

**Keywords:** polymer template; metal oxide semiconductor; one-dimensional; gas sensing performance

check for updates

Academic Editor: Jin-Ming Wu

Received: 9 August 2025
Revised: 30 September 2025
Accepted: 3 October 2025
Published: 7 October 2025

**Citation:** Nkuna, K.S.; Mokhena, T.C.; Erasmus, R.; Shingange, K. Polymer Template Selection for 1D Metal Oxide Gas Sensors: A Review. *Processes* **2025**, *13*, 3180. https://doi.org/10.3390/pr13103180

**Copyright:** © 2025 by the authors. Licensee MDPI, Basel, Switzerland. This article is an open access article distributed under the terms and conditions of the Creative Commons Attribution (CC BY) license (https://creativecommons.org/licenses/by/4.0/).

## 1. Introduction

Modern advancements in industrialisation and urban development have significantly enhanced the quality of life by enabling the establishment of advanced infrastructure, facilities, and services [1]. However, this progress has concurrently increased the emission of hazardous toxic gases into the atmosphere, posing serious risks to environmental sustainability and human health [1]. Consequently, the effective detection and monitoring of these gases are imperative, rendering gas sensing technologies critical for pollution control and safeguarding public safety [1]. Central to the functionality of any gas sensor is the sensing layer, whose material composition and structural characteristics critically determine key sensor performance parameters such as sensitivity, selectivity, response time, and long-term stability [2].

Metal oxide semiconductors (MOSs) have been extensively investigated as sensing materials due to their chemical robustness, thermal stability, and favourable electrical properties [3]. Notably, the dimensionality of these MOSs, ranging from zero through to three-dimensional (0–3D) nanostructures, as displayed in Figure 1, has a profound influence on their gas sensing efficacy [2]. One-dimensional (1D) MOS nanostructures, for example, nanowires, nanotubes, and nanorods, have garnered considerable attention as highly effective sensing layers [4]. Their unique morphology provides a high surface-to-volume ratio, enhancing gas adsorption and facilitating accelerated electron transport, which jointly contribute to heightened sensitivity and rapid sensor response [4]. The ability to precisely control these 1D morphologies enables optimisation of material properties to achieve lower detection limits for a broad range of toxic gases.

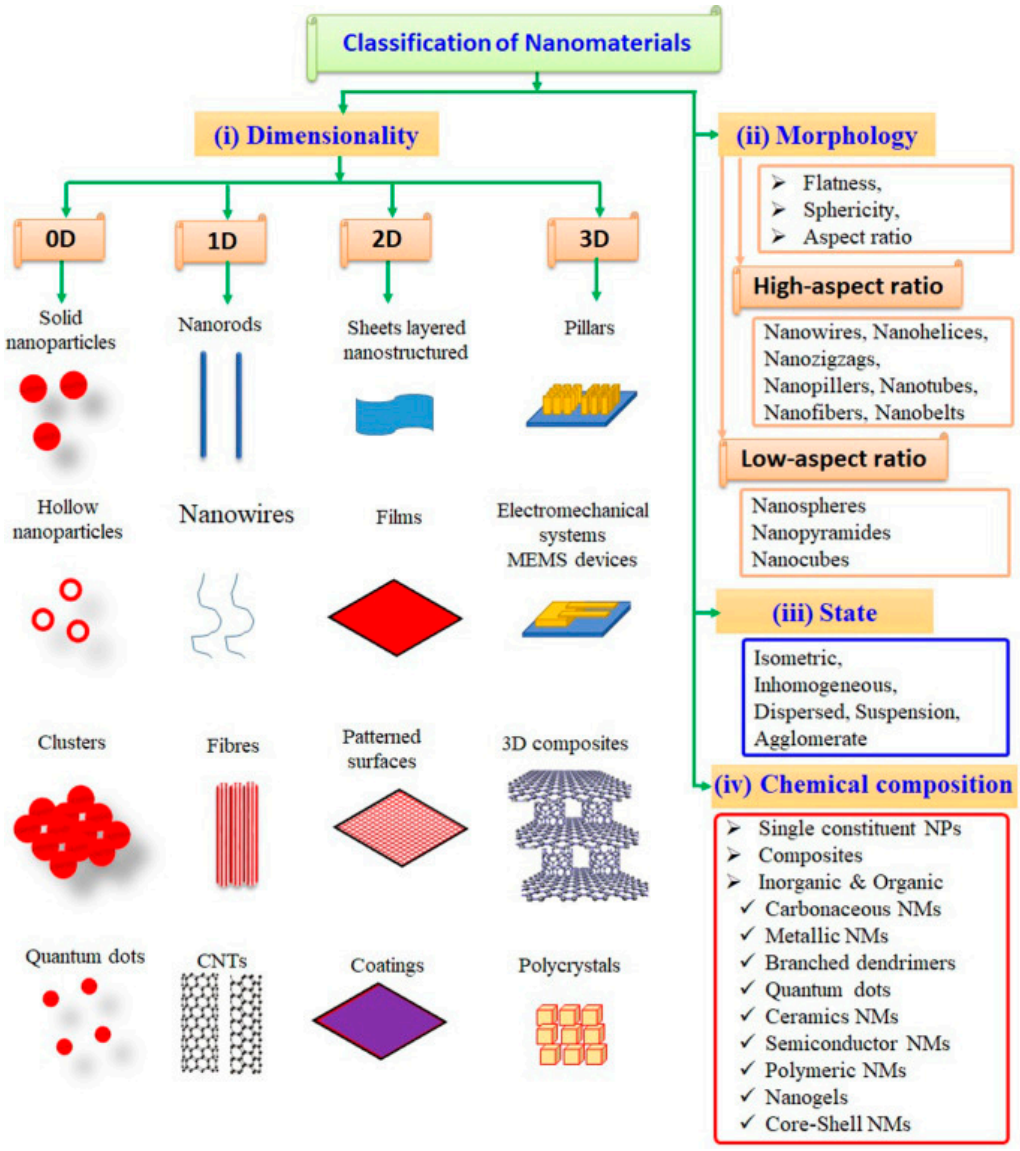


**Figure 1.** Classification of nanomaterials in their respective dimensions, ranging from 0D to 3D and everyday examples, reproduced with permission from Saleh [5], Environmental Technology & Innovation, published by Elsevier 2020.

Despite these advantages, pristine MOS nanostructures frequently face limitations such as agglomeration, poor dispersibility, and restricted surface functionalisation, which can impair sensing performance [4]. In this regard, polymeric templates play a crucial role in overcoming these challenges. Polymers function as adaptable scaffolds, directing the

synthesis of uniform 1D MOS nanostructures with controlled dimensions and porosity [6]. Beyond templating, polymer matrices can also modulate the electronic environment and surface chemistry of metal oxides, thereby enhancing gas adsorption sites and facilitating charge transfer mechanisms [6]. Such polymer–metal oxide hybrid composites often exhibit superior mechanical flexibility, enhanced stability, and improved sensitivity compared to their pure MOS counterparts [6].

Recent studies have demonstrated the instrumental role of polymeric templates in the fabrication of 1D MOS nanostructures with superior gas sensing properties. For instance, electrospun polymer nanofibres have been employed as sacrificial templates to produce ultrathin MOS nanofibres with exceptional responses to hydrogen sulphide ($H_2S$), attributable to their interconnected porous networks and high crystallinity [7,8]. Similarly, polymer-assisted hydrothermal synthesis has yielded well-defined ZnO nanowires exhibiting improved sensing behaviours towards $C_2H_2$ gas [9]. These advancements demonstrate the synergistic effect of polymeric templates in mitigating the drawbacks of conventional MOS fabrication approaches and advancing the development of next-generation gas sensors possessing tunable, highly efficient sensing layers.

The utilisation of polymeric templates to engineer 1D metal oxide nanostructured sensing layers presents a powerful strategy to enhance gas sensing performance. To the best of our knowledge, only a few reviews have addressed the use of polymeric materials as templates for the synthesis of one-dimensional nanostructures, with a clear correlation between the resulting structural properties and gas sensing performance [10–12]. Notably, the existing studies are dated to 2020 [10] and 2022 [11,12], highlighting the need for a comprehensive review that captures recent advances in 1D nanostructured materials and their gas sensing capabilities. This review critically evaluates recent progress in this area, emphasising fundamental principles, synthesis techniques, and the sensing capabilities of polymer-assisted 1D MOS systems. Viewed through this lens, polymeric materials not only serve as fabrication facilitators but also emerge as key enablers of augmented sensor functionality, thereby paving the way for innovative applications in environmental monitoring, industrial safety, and healthcare diagnostics.

## 2. Fundamentals of 1D MOS Gas Sensors

The field of gas sensing has witnessed substantial progress with the advent of 1D MOS nanostructures. These materials, commonly designed as nanowires, nanorods, and nanotubes, exhibit unique physical, electronic, and chemical features that render them highly appealing for advanced gas sensing applications. Understanding the fundamentals of 1D MOS gas sensors necessitates an exploration of their core structural, morphological, electronic, and optical properties, as each directly influences sensor performance.

### *2.1. Structural Properties*

At the atomic scale, 1D nanostructures are characterised by well-ordered lattices that can be either single-crystalline or polycrystalline, depending on the synthesis route employed. High crystallinity, as seen in many hydrothermally grown ZnO in Figure 2 or $SnO_2$ nanowires, is highly desirable because it minimises grain boundaries that act as trapping sites for charge carriers [13]. The reduced presence of such defects facilitates enhanced charge transport, crucial for achieving rapid and sensitive gas detection [13].

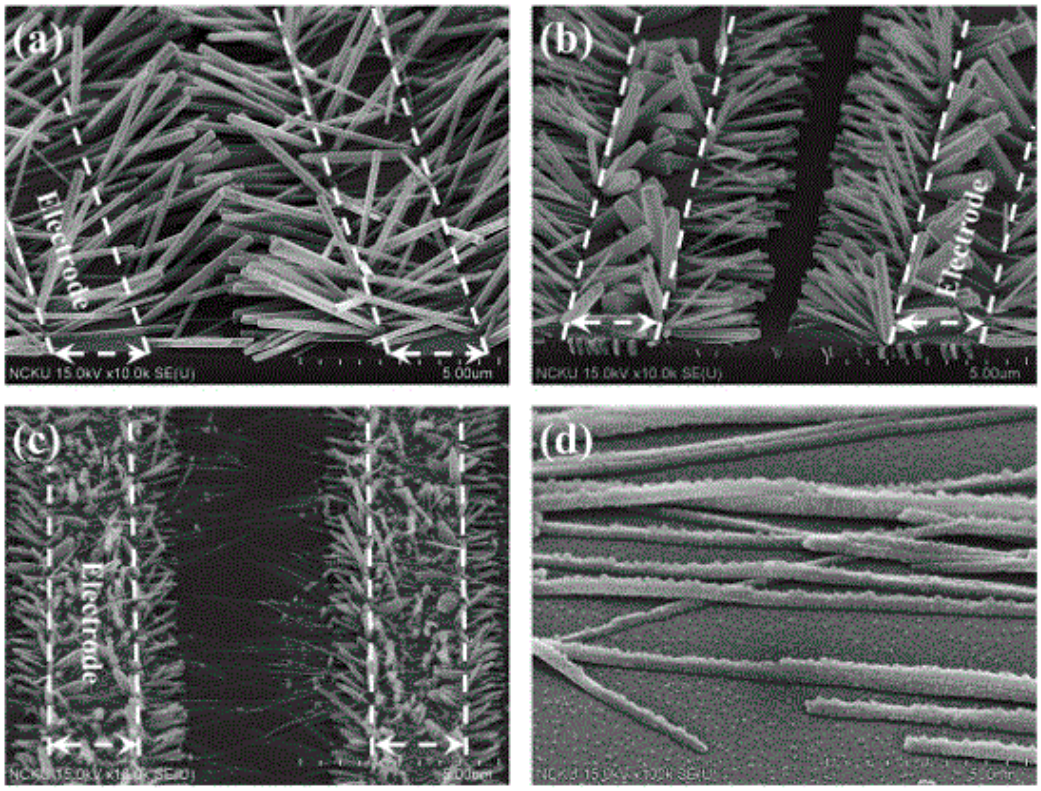


**Figure 2.** The SEM images of highly crystalline ZnO nanowires synthesized via hydrothermal method under different solution concentration and growth duration; (**a**) 10 mM and 1 h, (**b**) 5 mM and 1 h, (**c**) and (**d**) 1 mM and 6 h. Reproduced with permission from Sen et al. [14], Thin Solid Films; published by Elsevier, 2016.

The nature of the crystal lattice strongly influences sensor performance. For example, $SnO_2$ commonly crystallises in the rutile phase [15], while ZnO typically forms a wurtzite lattice structure [16]. These distinct crystal structures impact the density and type of intrinsic defects, such as oxygen vacancies, which serve as active sites for gas adsorption and interaction. In ZnO nanorods, the wurtzite structure combined with high crystalline quality leads to efficient electron mobility and surface reactivity, enabling sensitive detection of gases like Nitrogen dioxide ($NO_2$) [17]. Similarly, rutile $TiO_2$ nanowires with tailored crystallinity exhibit excellent stability and reproducible sensor responses towards VOCs [18]. Thus, controlling the crystal phase and quality directly affects the electronic properties underpinning sensor performance.

Dimensional parameters, including diameter, length, and aspect ratio (length-to-diameter), play a crucial role in defining the sensing behaviour of 1D MOS nanostructures [19]. Nanostructures with smaller diameters inherently possess a higher surface-to-volume ratio, which maximises the number of active adsorption sites available for gas molecules [17]. This effect enhances sensitivity significantly because the charge carrier modulation induced by gas adsorption occurs predominantly at the surface. According to Cai et.al [20] ultrathin Selenium–Tin (Se-Sn) nanofibers fabricated via electrospinning with diameters below 100 nm show markedly improved gas sensing performance due to their large accessible surface area and porous morphology. These nanofibers exhibit high sensitivity and selectivity toward triethylamine (TEA), owing to their enhanced surface-to-volume ratio and effective electron transport pathways enabled by the ultrathin and porous structure. The aspect ratio is equally important, particularly when these nanostructures are employed as single-element sensors or in networks where conduction pathways are

established along their length. High aspect ratios facilitate efficient electron transport, enabling fast and amplified changes in electrical resistance upon gas exposure.

### 2.2. Morphological Properties of 1D MOS for Gas Sensing

The morphology of 1D MOS nanostructures plays a fundamental role in determining their gas sensing characteristics. Key morphological features such as surface topography, porosity, uniformity, and defect structure influence how gas molecules interact with the sensor surface, impacting sensitivity, selectivity, response time, and stability.

#### 2.2.1. Surface Topography and Porosity

Surface roughness and porosity profoundly affect the density of accessible active sites for gas adsorption [21]. Rough, porous structures increase surface area and provide pathways that facilitate the penetration and diffusion of gas molecules deep into the sensing layer, rather than restricting interactions to the external surface [21]. For instance, electrospun MOS nanofibers such as $LaCoO_3$ [22], ZnO [23], and $In_2O_3$ [23] exemplify the benefits of enhanced surface morphology. $LaCoO_3$ nanofibers produced by electrospinning polymer templates followed by calcination at different temperatures exhibited a highly porous, interconnected network with fibers below 58 nm in diameter. This high surface-to-volume ratio significantly improves the adsorption of ethanol, translating to faster and stronger sensor responses [24]. Similarly, porous ZnO nanofibers fabricated through electrospinning demonstrate increased sensitivity to reducing gases such as $H_2$, CO, and $CH_4$, attributable to the hierarchical pore structures that accelerate gas diffusion and interaction kinetics, thereby enhancing the surface reaction rate and improving overall sensing performance [25].

Template-assisted synthesis methods further enable the engineering of precise nanoscale morphologies [26]. For example, $TiO_2$ nanotube arrays created by electrochemical anodization polymer templating possess uniform vertical alignment and nanoscale pore diameters [25]. These architectures provide a vast active surface area coupled with rapid gas diffusion channels, enhancing sensor response and recovery times while maintaining structural robustness. Post-synthesis treatments like annealing or acid etching can fine-tune pore size and surface roughness, further optimizing gas accessibility and sensor performance.

#### 2.2.2. Homogeneity and Defect Sites

Achieving morphological uniformity is crucial for sensor consistency and selectivity. Uniform 1D nanostructures with well-defined diameters, lengths, and surface properties ensure reproducible sensor output by reducing variability in electron transport and gas interaction pathways [4]. Techniques such as vapour-liquid-solid (VLS) growth of ZnO nanowires and nanorods have successfully produced highly monodisperse arrays that exhibit stable and selective detection of gas analytes, demonstrating the importance of controlled morphology [4,27,28].

Conversely, deliberate introduction of controlled defects can enhance sensor sensitivity and selectivity. Defects in materials are irregularities or disruptions in the regular arrangement of atoms within a crystal lattice. These imperfections can significantly influence the physical, chemical, electronic, and optical properties of the material. Defects play a crucial role in determining the gas-sensing performance of materials [29,30].

Oxygen vacancies, for example, are one of the most critical morphological defects intrinsically linked to MOS gas sensing mechanisms. These vacancies act as electron donors, creating localized sites favorable for the adsorption of gas molecules [31]. Photoluminescence (PL) has been widely applied to study the defect structures in transition in MOS materials [32–34].

When exposed to an excitation source with photon energy equal to or greater than the band gap, MOS nanocrystals absorb the photons, leading to the generation of photo-excited electrons in the conduction band and holes in the valence band. These electron-hole pairs, known as excitons, subsequently recombine at defect sites, producing trap-state luminescence. PL is therefore a valuable tool in gas sensing research for probing defect-related properties in MOS-based sensors. In addition to PL, other complementary techniques such as cathodoluminescence (CL), electron paramagnetic resonance (EPR), X-ray photoelectron spectroscopy (XPS) and Raman spectroscopy are also commonly employed to investigate and analyze defect structures in these materials [30,35–39]. Mhlongo et al. [32] demonstrated that higher oxygen vacancy concentrations not only enhanced gas sensing but also induced room-temperature ferromagnetism, linking defect-mediated magnetism with sensing performance. The correlation was established through a combination of techniques, including PL to track defect-related emissions, XPS to quantify oxygen-vacancy contributions in the O 1 s spectrum, EPR as an indirect probe of vacancy-induced ferromagnetism, and direct gas sensing measurements. These results highlights the central role of oxygen vacancies and highlight the effectiveness of multi-technique approaches in clarifying structure–property relationships in MOS-based sensors.

Enhanced vacancy concentration within ZnO nanorods [40,41] or $SnO_2$ nanowires [42] has led to improved sensitivity and faster response times at room temperature, a significant advantage for practical applications.

In addition to intrinsic defects, doping or surface decoration with metal nanoparticles (such as Pd, Pt, or Au) can introduce catalytic sites and heterojunctions that improve charge transfer and catalytic oxidation/reduction reactions at the sensor surface [43–45]. Au-functionalized ZnO nanorods, for example, demonstrated ammonia ($NH_3$) by facilitating $NH_3$ spillover effects on the ZnO surface [46]. These dopants and defects create active centers that specifically enhance gas molecules adsorption or reaction kinetics, boosting sensor performance.

Balancing defect concentration is essential since excessive defects may increase charge carrier recombination or degrade stability [31]. Synthesis approaches such as controlled atmosphere annealing and polymer-template-assisted growth allow for fine control of morphology and defect density to tune sensor performance toward the desired balance of sensitivity and longevity.

### *2.3. Electronic Properties*

The electronic properties of 1D MOS nanostructures are fundamental to their outstanding gas sensing performance, as they govern the conversion of gas adsorption events into measurable electrical signals [11]. Typically, many MOS materials such as ZnO, $TiO_2$, and $SnO_2$ behave as n-type semiconductors, where electrons serve as the primary charge carriers. However, p-type MOS materials like NiO, CuO, and $Co_3O_4$ have also gained interest for complementary sensing applications. The sensing mechanism principally involves modulation of the electrical conductivity or resistance of the nanostructure due to changes in surface charge carrier density induced by gas adsorption [11]. In ambient conditions, oxygen molecules adsorb onto the MOS surface and capture conduction band electrons, creating an electron depletion layer [11]. The extent of this depletion layer is sensitive to interactions with target gases. Exposure to reducing gases such as $H_2$ or CO results in the reduction of adsorbed oxygen ions and releases electrons back to the conduction band, decreasing the depletion width and lowering resistance [3]. Conversely, oxidising gases like $NO_2$ extract additional electrons from the surface, deepening the depletion region and increasing resistance [3].

The 1D morphology of these nanostructures plays a critical role in amplifying this effect because their diameters often approach or are smaller than twice the depletion layer thickness, meaning gas-induced surface charge changes influence the entire cross-section. This results in significant and rapid variations in electrical resistance, enabling the detection of gases at very low concentrations. Additionally, the high crystalline quality and long-range order in single-crystalline nanowires minimize electron scattering, supporting swift charge transport and fast sensor response times [47,48].

Surface electronic states, including those arising from intrinsic defects, dopants, and heterojunctions, profoundly affect the sensing behavior by altering charge carrier dynamics and surface reactions [48]. Oxygen vacancies, common intrinsic defects, act as shallow donors supplying free electrons and serve as preferred adsorption sites for gas molecules, particularly oxidising species [48]. Manipulating oxygen vacancy concentration through controlled synthesis or post-treatment can thus tailor sensor sensitivity and selectivity. Further enhancement arises from doping or surface decoration with transition metals (e.g., Fe, Mn) or noble metals (e.g., Au, Pd, Pt). Noble metal nanoparticles deposited on MOS nanostructures act as catalytic centers, facilitating gas molecule dissociation and electron exchange via spillover effects that accelerate surface reactions and reduce activation energies. For example, Pd-functionalized $SnO_2$ nanofibers exhibit ultrahigh butane sensing sensitivity and selectivity because Pd efficiently dissociates butane, promoting rapid electron transfer to the $SnO_2$ surface and markedly modulating its resistance [49]. Moreover, heterojunction formation between different MOS materials or with other semiconductors introduces potential barriers that modulate charge carrier transport; gas exposure alters these barriers and amplifies the sensing signal [50]. ZnO-$TiO_2$ heterostructured nanorods illustrate this effect, offering superior sensitivity and rapid response to ammonia gas due to synergistic band alignments enhancing electron transfer and surface reactions [51].

### *2.4. Optical Properties*

One-dimensional MOS nanostructures exhibit unique optical properties that are integral to their function and enhancement in gas sensing applications. These properties arise primarily from their reduced dimensionality, high surface-to-volume ratio, and quantum confinement effects [52]. When the characteristic dimensions of these nanostructures approach or fall below the exciton Bohr radius, quantum confinement leads to an increase in band gap energy compared to their bulk counterparts, effectively resulting in blue-shifted absorption edges [52]. For example, ZnO nanorods and $SnO_2$ nanowires with diameters smaller than 50 nanometres show such band gap broadening, which modifies their photon absorption and emission characteristics [53,54]. These alterations in optical properties facilitate the use of 1D MOS nanostructures in optical gas sensing techniques, where gas adsorption induces measurable changes in photoluminescence intensity, optical absorbance, or Raman scattering [52]. Adsorption-driven variations in local surface states or charge transfer processes modulate these optical signals, providing an additional, often complementary, transduction mechanism alongside conventional electrical detection.

Furthermore, many 1D MOS materials demonstrate intrinsic photocatalytic activity under ultraviolet or visible light illumination [55]. Photon absorption excites electrons from the valence to the conduction band, generating electron–hole pairs that migrate to the surface and participate in chemical reactions with adsorbed gas molecules [55]. This photoactivation enhances surface reaction kinetics, thereby improving sensitivity and enabling sensor operation at or near room temperature, which is an essential advancement over traditional high-temperature MOS sensors.

In addition to electrical and photocatalytic effects, modern sensor designs increasingly leverage integrated multi-modal transduction approaches, where both optical and electrical

responses are simultaneously monitored [56]. This hybrid strategy exploits the complementary nature of electron transport modulation and optical signal variation upon gas adsorption, enhancing sensitivity and selectivity. Similarly, devices utilizing whispering gallery mode optical resonators coated with 1D MOS nanostructures capitalize on shifts in optical resonance wavelengths induced by gas adsorption-related refractive index changes, achieving highly sensitive and rapid gas detection [56]. Integration of polymer matrices with MOS nanostructures further facilitates flexible optical sensor platforms with enhanced molecular recognition and optical clarity, thereby improving overall sensor robustness and functionality [52,56].

## 3. Gas Sensing Mechanism and Contributing Factors

There are different types of gas sensors, including MOS, Fluorescence, electrochemical, and IR sensors (see Figure 3), each designed to detect specific gases or groups of gases. These sensors operate based on different underlying principles and mechanisms, depending on the type of gas they are intended to detect. Thus, their working principles vary, with each type employing a unique sensing technology to function effectively. This is like what is observed in MOS gas sensors, which operate based on the principle of chemoresistance, where the electrical resistance of the material changes depending on the type and concentration of the gas present [1].

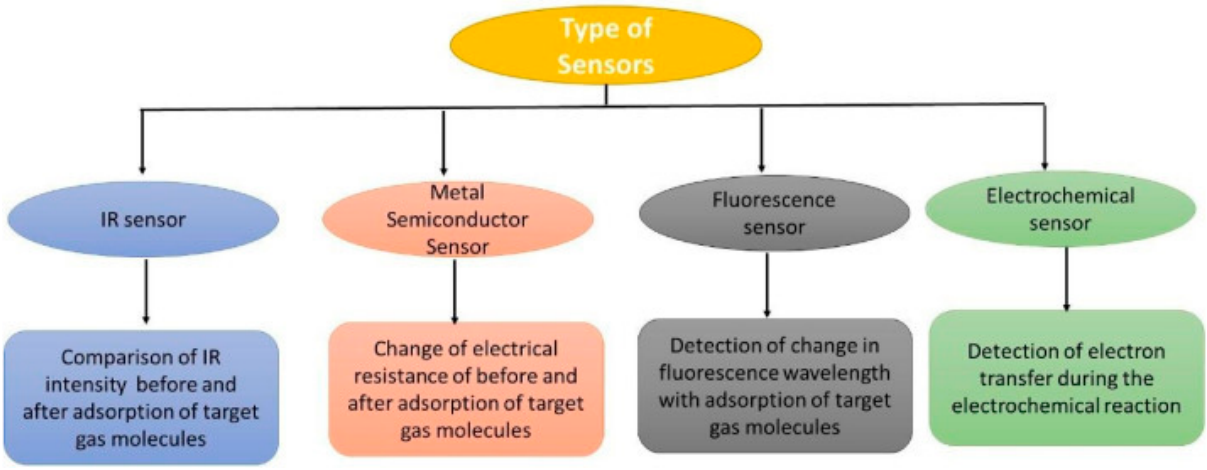


**Figure 3.** Some types of gas sensors and their underlying principle, reproduced with permission from [57].

It has long been accepted that the gas-sensing mechanism of MOS is primarily based on oxygen adsorption. However, this view has been challenged in recent years by several researchers. For instance, N. Goel et al. [2] emphasise that the operating temperature plays a crucial role in influencing the sensing mechanism of these materials. MOS can be categorized based on their operating temperature into two types: surface-conductance-based materials, which are typically oxide-based and operate at low to moderate temperatures below 600 °C, and bulk-conductance-based materials, which function at higher temperatures, generally above 700 °C [2,3].

The sensing mechanism of the MOS is further categorized at the microscopic and macroscopic levels. The microscopic levels support different mechanisms like Fermi-level control theory and charge carrier depletion layer theory, while the macroscopic level focuses on adsorption/desorption processes, bulk resistance control mechanism, and gas diffusion control mechanisms [2]. Typically, in MOS-based gas sensors, the macroscopic is preferred because the focus is more on overall sensor performance, such as sensitivity, response time, and stability, than on microscopic interactions [29].

MOS-based gas sensing devices are primarily influenced by chemical adsorption and desorption, as this is the dominant mechanism governing their sensing behaviour. Chemical adsorption (chemisorption) involves the formation of strong chemical bonds between the adsorbate and the adsorbent, making it a specific and often irreversible process [1]. Desorption, the reverse process, requires breaking these bonds and is influenced by factors such as temperature and surface properties [58,59].

MOS sensors can be classified into n-type and p-type based on their dominant charge carriers: electrons for n-type and holes for p-type [60]. These two types respond differently when exposed to a target gas. When the gas comes into direct contact with the sensor surface, a chemical reaction occurs, leading to a fluctuation in the electrical signal. This happens because the target gas either donates or accepts electrons during the surface interaction, which alters the charge carrier concentration and causes a measurable change in the resistance of the sensor [3]. This reaction is summarized in Table 1, which shows how the interaction between the target gas and the MOS surface leads to either an increase or a decrease in resistance, depending on the type of gas and whether the material is n-type or p-type [61].

**Table 1.** Surface reaction effects on n-type and p-type MOS Sensors.

| Gas Type | Reaction Type | Electron Flow | Effect on n-Type MOS | Effect on p-Type MOS |
|---|---|---|---|---|
| Reducing gas (e.g., CO, $H_2$, $NH_3$). | Oxidation of gas. | Releases electrons into MOS. | Resistance decreases. | Resistance increases. |
| Oxidizing gas (e.g., $NO_2$, $O_3$, $Cl_2$). | Reduction of gas. | Withdraws electrons from MOS. | Resistance increases. | Resistance decreases. |

According to Padvi et al. [61], an ideal gas sensor should exhibit high sensitivity and selectivity, good stability, a long-life cycle, low operating temperature, and fast response and recovery times. These factors are central, as they can either enhance the functionality of the sensor or limit its effectiveness, preventing it from meeting the criteria of an ideal gas sensor [2,61]. When designing ideal gas sensors, it is essential to take key performance parameters into account. One of the most important of these is sensitivity, which refers to the ability of the sensor to detect the presence of gases. Factors such as the composition and properties of the sensing material, as well as the operating temperature, especially at room temperature, must be considered when assessing the sensitivity of the sensor [2,3,29].

There are numerous gases present in the atmosphere, but an ideal gas sensor should be capable of detecting the target gas even in the presence of other interfering gases. This characteristic is referred to as selectivity [3]. To ensure the accuracy of the sensor's output, high selectivity is essential. Another critical parameter is stability, which refers to the ability of the sensor to deliver consistent and reliable readings over an extended period [29]. However, this is often a limiting factor in MOS sensors [2,3,29].

Response time is defined as the duration between the moment when the gas concentration reaches a certain level and when the sensor produces a corresponding signal [29]. In contrast, recovery time refers to how long the sensor takes to return to 90% of its original signal after the removal of the target gas [29]. Gas sensors that operate at room temperature are preferred for many real-world applications due to their low power consumption, enhanced durability, and ease of portability. However, most MOS-based gas sensors require elevated temperatures to initiate the adsorption/desorption processes on the sensing surface [2,3,29].

## 4. Polymeric Template Selection, Synthesis, and Gas Sensing Performance

Polymeric materials play a crucial role in the development of advanced gas sensors due to their versatile chemical structures, ease of synthesis, and tunable properties. The selection of appropriate polymers is fundamental to optimizing the sensor's performance, including sensitivity, selectivity, and stability. By carefully designing polymer matrices and incorporating functional groups, researchers can tailor interactions with specific gas molecules, enhancing the overall detection capabilities. The synthesis methods employed significantly influence the morphological features of the polymers, which in turn affect their gas sensing behavior.

The unique properties of 1D MOS, together with their ability to confine charge carrier transport along a single axis, lead to enhanced charge mobility and heightened sensitivity, making them exceptionally effective for detecting gas molecules. Moreover, hollow 1D MOS nanostructures offer improved adsorption and desorption kinetics, resulting in faster sensor response and recovery times. Integrating these 1D MOS with polymeric materials combines the benefits of both, leading to superior gas sensor performance.

### *4.1. Polymetric Template Selection*

Polymeric templates are structures used to guide the formation of polymers with specific properties and configurations [62]. These templates can be made from various materials, including Deoxyribonucleic Acid (DNA), Ribonucleic Acid (RNA), hydrogels, and metal-organic frameworks (MOFs) [63]. By acting as precise scaffolds, polymeric templates enable the control of size, shape, and arrangement of polymers, which is essential for developing materials with tailored functions across many scientific and technological fields [6,63,64].

Polymeric templates are broadly classified into two categories: natural and synthetic polymers. Both types play essential roles in various applications due to their unique properties. Table 2 summarizes the different types of polymers, highlighting their key properties and their uses across multiple fields. Polymeric templates play a crucial role in shaping the structure, pore size, and surface area of 1D MOS by effectively controlling the material formation process, which directly impacts their performance [65]. The morphology can be finely tuned by adjusting parameters including polymer concentration, molecular weight, and infiltration conditions. Furthermore, microwave annealing accelerates the infiltration process and provides superior control over the morphology compared to conventional thermal treatments [6,66]. In terms of porosity control, the resultant porosity is influenced by both the type of polymer used and the synthesis technique employed [67,68]. For instance, employing polyesters combined with sequential vapor infiltration (SVI) allows for the precise tuning of micro- and mesoporous structures [68]. Block copolymers (BCPs), in particular, create more open surface architectures relative to intrinsic microporous polymers such as PIM-1 [69]. Surface area control is achieved through methods such as utilizing anodic aluminium oxide (AAO)-based polymer templates that replicate complex surface morphologies, thereby enhancing surface area [66]. The use of swollen polymers as templates produces porous materials with high surface areas, making them well suited for catalytic and separation applications [70]. Moreover, interactions between the polymer template and MOS influence the physical characteristics of the composite, which can improve selectivity and overall material gas sensing performance [70].

**Table 2.** Overview of natural and synthetic polymeric templates [70–73].

| Type | Polymer | Properties | Applications |
| --- | --- | --- | --- |
| Natural | Chitosan | Biodegradable, biocompatible, antimicrobial | Drug delivery, porous structures |
| | Alginate | Water-soluble, forms gels, high ion exchange capacity | Tissue engineering, hydrogels |
| | Cellulose | Abundant, biodegradable, high tensile strength | Nanocomposites, nanostructures |
| | Gelatin | Biocompatible, forms hydrogels, high water affinity | Drug delivery, porous structures |
| Synthetic | Polystyrene | Rigid, transparent, good chemical resistance | Microspheres, nanostructures |
| | Polyvinyl Alcohol (PVA) | Water-soluble, biodegradable, good film-forming properties | Drug delivery, porous materials |
| | Polylactic Acid (PLA) | Biodegradable, biocompatible, good mechanical properties | Tissue engineering, scaffolds |
| | Polyvinylpyrrolidone (PVP) | Water-soluble, biocompatible, excellent film-forming | Drug delivery, stabilizers |

### *4.2. Synthesis Strategies*

Various fabrication techniques, such as thermal evaporation, self-catalytic growth, hydrothermal synthesis, and electrospinning, have been employed to produce 1D MOS [73,74]. Among them, electrospinning stands out for its simplicity, scalability, and efficiency in producing 1D nanostructures, commonly referred to as nanofibers [74–76]. These nanofibers exhibit a fibrous morphology with diameters ranging from a few nanometers to several microns, depending on factors such as solution composition, processing parameters, and environmental conditions. In the case of MOS-based nanofibers, their structural attributes are primarily influenced by the composition of the spinning solution and the electrospinning conditions. Therefore, optimizing these parameters is essential to achieve the desired nanofiber architecture.

The selection of an appropriate polymer is critical, as the electrospinnability of the solution depends on the molecular weight of the polymer and its ability to provide suitable viscosity. Compatibility between the polymer and the metal salt precursor is also essential, as it enhances the homogeneity and stability of the spinning solution. Post-electrospinning, the sacrificial polymer must be removed to yield pure MOS nanofibers. Calcination is the most employed method for this purpose, and its parameters, particularly temperature and duration, play a pivotal role in determining the final properties of the nanofibers. Table 3 summarizes studies based on 1D MOS nanofibers [75,77,78].

Calcination can significantly affect the crystallinity, morphology, and surface area of the resulting MOS structures—for example, Liming et al. [79] reported that increasing the calcination temperature from 400 °C to 600 °C transformed the material from an amorphous to a crystalline phase, thereby enhancing its gas-sensing performance toward ethylene glycol at room temperature. Achieving optimal crystallinity is essential for enhancing gas sensing performance. Higher calcination temperatures and longer calcination durations

typically improve crystallinity, which in turn reduces the number of charge carriers. This reduction enhances the modulation of electrical resistance during gas adsorption and desorption, resulting in improved sensor responses. Additionally, 1D MOS produced under these conditions often consists of nanograins. As calcination temperature and time increase, these nanograins tend to coalesce and grow, altering the physical and chemical properties of the nanofibers [24]. Larger grains reduce the number of grain boundary barriers, leading to a less pronounced resistance modulation and, consequently, diminished sensing performance. For example, $SnO_2$ nanofibers with smaller grains have demonstrated superior CO sensing capabilities compared to those with larger grains, due to the increased number of potential barriers at grain boundaries that enhance resistance modulation [80]. Conversely, ZnO-based 1D materials with larger grains have shown better sensing performance than those with smaller grains [81,82], highlighting that the optimal grain size for sensing can vary depending on the material system.

Hollow nanotubes can also be fabricated using the electrospinning technique [83,84]. The production of these nanotubes has been reported to depend on several factors, including the composition of the precursor solution, the electrospinning parameters, and the specific electrospinning technique employed. The first approach involves electrospinning a polymeric material without incorporating a metal precursor, followed by coating the resulting fibers with the precursor [62,84,85]. Subsequent thermal decomposition of the polymer template then yields hollow nanotubes. In a study by Cho et al. [85], electrospun fibers were used as templates to facilitate the formation of hollow nanotubes. The authors electrospun a blend of PVP and PMMA, producing fibers with diameters ranging from 400 to 600 nm. These fibers were then coated with a 50 nm $SnO_2$ overlayer via sputtering. Subsequent calcination at 450 °C for 30 min resulted in the formation of hollow submicron tubes. Transmission electron microscopy (TEM) images revealed hollow nanofibers with diameters between 300 and 500 nm and shell thicknesses of approximately 15–20 nm. The resulting polycrystalline $SnO_2$ structure exhibited grain sizes of around 10 nm. In another study, the hollowness of ZnO nanotubes was investigated by varying the concentration of the polymer in the electrospinning solution. As polymer concentration increases, so does the viscosity, resulting in the formation of thicker fibers. The authors coated these fibers, produced at different diameters, with a ZnO precursor to create hollow nanotubes with varying inner diameters. It was observed that the diameter of the hollow core increased from 50 nm to 185 nm as the polymer concentration in the spinning solution rose from 5.5% to 9.0%. Smaller hollow diameters resulted in enhanced performance, attributed to the increased surface area available for interaction. The method has demonstrated potential for fabricating hollow hybrid nanotubes suitable for gas-sensing applications [86]. Han et al. [86] employed a combination of electrospinning and atomic layer deposition (ALD) to synthesize p-CuO/n-ZnO nano-heterojunction hollow tubes (Figure 4a). Initially, a spinning solution containing PVP and $Cu(CH_3COO)_2 \cdot H_2O$ was electrospun into nanofibers, which were subsequently coated with ZnO using ALD with diethyl zinc (DEZn) and $H_2O$ as precursors. The ZnO coating thickness, ranging from 44 to 120 nm, was controlled by adjusting the number of ALD cycles. The coated fibers were then annealed at 550 °C for 2 h with a heating rate of 1 °C/min to form hollow nanotubes. XRD analysis confirmed the presence of both monoclinic CuO and hexagonal wurtzite ZnO phases (Figure 4b). SEM images revealed ultra-long, hollow nanofibers with smooth surfaces (Figure 4c–e), and the wall thickness of the nanotubes ranged from 45 to 126 nm (Figure 4f–h). High-resolution imaging showed lattice spacings of 0.260, 0.281, and 0.252 nm, corresponding to the (002) and (100) planes of ZnO and the (111) plane of CuO, respectively (Figure 4i). Elemental mapping indicated uniform distribution of Zn, Cu, and O across the nanotube shells, suggesting diffusion of CuO nanoparticles toward the outer surface during calcination

(Figure 4i–l). This demonstrates that by selecting appropriate techniques and precursors, it is possible to precisely control the shell size and composition, enabling the fabrication of tailored materials for gas-sensing applications.

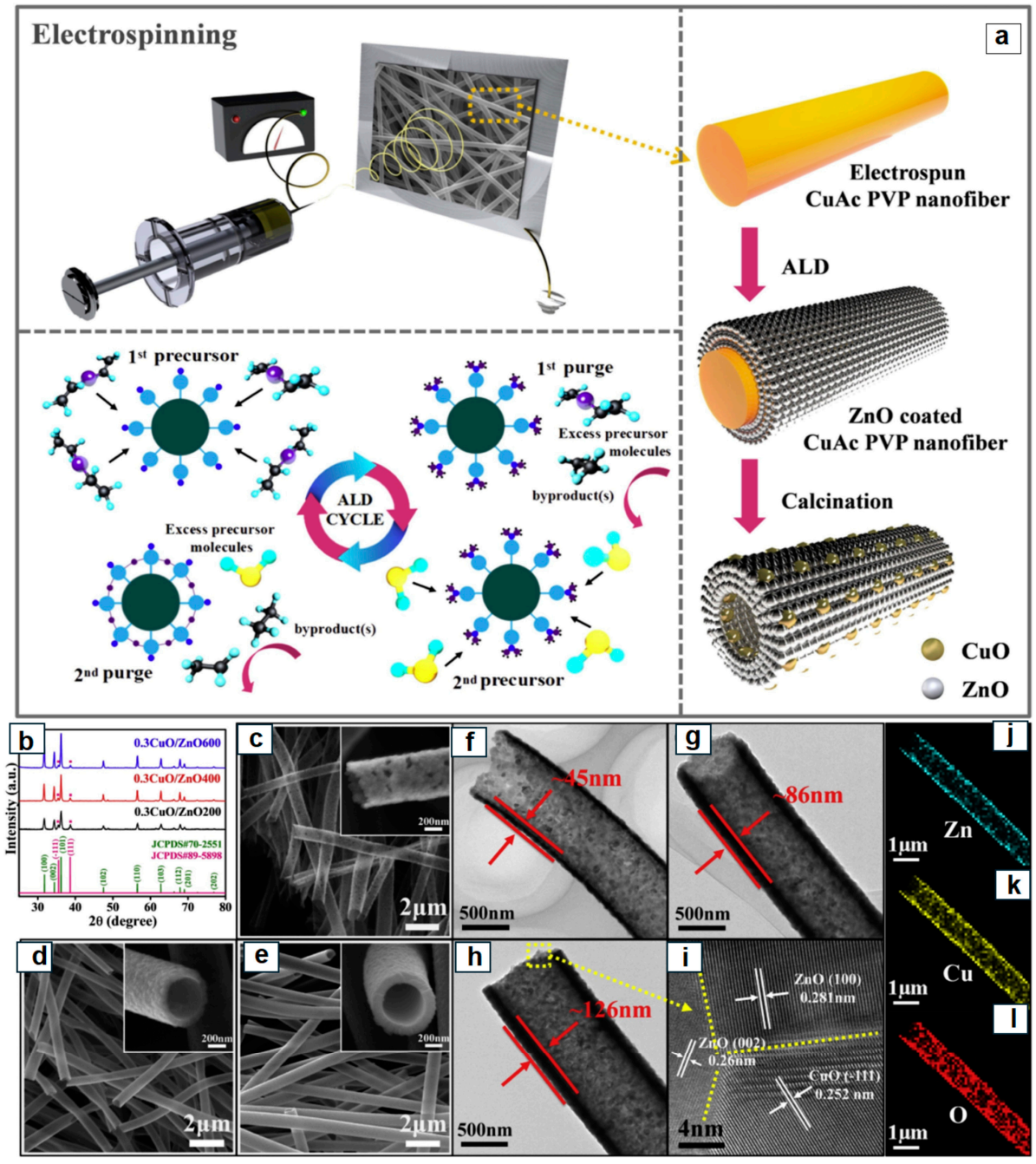


**Figure 4.** (**a**) Schematic illustration of the heterojunction hybrid nanotube fabrication process using a three-step method: electrospinning, coating, and calcination. (**b**) XRD patterns of CuO/ZnO heterojunction hybrid hollow nanotubes. (**c**–**e**) SEM images, (**f**–**h**) TEM images, and (**i**) HRTEM image of the CuO/ZnO hybrid hollow nanotubes. (**j**–**l**) Elemental mapping images showing the distribution of Cu, Zn, and O in the hybrid nanotube shells. Reproduced with permission from Han et al. [86], Sensors and Actuators B: Chemical; published by Elsevier, 2019.

Li et al. [87] synthesized hollow ZnO-$SnO_2$ nanotubes using a two-step process. In the first step, $SnO_2$ precursor was electrospun in the presence of a template polymer, followed by annealing to form hollow $SnO_2$ nanotubes. These pre-formed nanotubes were then immersed in a ZnO precursor solution and subjected to a hydrothermal treatment, resulting

in ZnO growth on the surface of the hollow $SnO_2$ tubes. The resulting ZnO-$SnO_2$ hybrid nanotubes retained a similar morphology to the pristine $SnO_2$ tubes, as ZnO primarily filled the interstitial spaces between $SnO_2$ particles. The specific surface area and BJH adsorption average pore width of the ZnO-$SnO_2$ hybrids increased from 2 $m^2/g$ to 34 $m^2/g$ and from 25 nm to 27 nm, respectively, compared to the neat $SnO_2$ nanotubes. This enhancement was attributed to the hydrothermal process, which reduced crystallite size and improved nanoparticle dispersion. The study concluded that the increased surface area and broader pore distribution were due to partial substitution of $Sn^{4+}$ sites by $Zn^{2+}$ ions. Similarly, Tian et al. [88] successfully synthesized hollow ZnO nanotubes via electrospinning, followed by hydrothermal decoration with ZIF-8 at 80 °C for 3 h. These hybrid materials are particularly valuable for gas-sensing applications due to the unique properties of MOFs. MOFs are distinguished by their tunable porosity and high crystallinity, both of which are critical for achieving enhanced gas-sensing performance [89,90].

Seshendra Reddy et al. [91] employed electrospinning to fabricate hollow $SnO_2$ nanotubes for gas-sensing applications. A precursor solution containing $SnO_2$ and PVP as a sacrificial polymer was electrospun, followed by annealing to form hollow nanotubes. The resulting nanotubes were then immersed in a graphene oxide (GO) solution and air-dried. Subsequently, the samples underwent thermal annealing at 200 °C for one hour. The pristine $SnO_2$ nanotubes exhibited an average diameter of 25 $\pm$ 21 nm, while the GO-doped $SnO_2$ nanotubes showed an increased diameter of 116 $\pm$ 21 nm.

Alternatively, coaxial electrospinning can be employed to fabricate hollow nanotubes, as demonstrated by [92]. This technique involves the use of a spinneret equipped with two coaxial capillaries to produce core–shell composite fibers. The core material is subsequently removed, resulting in the formation of hollow nanotubes. Careful selection of both the core and shell polymers is essential to ensure that the resulting hollow structures possess the desired structural and physical properties. For example, hollow $SnO_2$ nanotubes were successfully synthesized by dissolving a precursor salt in a PVP solution for the core, while paraffin was used as the inner fluid [92]. The resulting fibers had diameters ranging from 400 to 750 nm. After calcination, the well-defined hollow structure was preserved, with a final diameter of approximately 430 nm. This indicates that the thermal decomposition of PVP and paraffin during calcination did not compromise the integrity of the 1D nanostructure, making this approach highly suitable for the production of hollow nanotubes. The hollow nanotubes exhibited enhanced gas sensing performance compared to their solid fiber counterparts, primarily due to their higher surface area, which allows for greater interaction with target gas analytes.

Yet, another practical approach for producing hollow nanotubes involves the use of a single-needle electrospinning technique. In this method, two immiscible polymers are co-electrospun, followed by calcination to form hollow structures. Ab Kadir et al. [93]. demonstrated this by preparing hollow $SnO_2$ fibers using a mixture of two polymer solutions: PVP containing a stannous chloride precursor, and polyacrylonitrile (PAN). Varying amounts of PAN were added to the PVP/stannous chloride solution before electrospinning. The resulting fibers had diameters ranging from 80 to 400 nm, depending on the concentration of PAN. After calcination, hollow nanotubes were obtained with diameters of approximately 80 nm and 250 nm for 1 mL and 2 mL PAN additions, respectively. Interestingly, the addition of 3 mL PAN led to the formation of fibers with multiple small hollow channels and an overall diameter of around 400 nm (Figure 5a–c). The formation of these hollow structures was attributed to the immiscibility and incompatibility between PVP and PAN, which, combined with elongational forces during electrospinning, induced phase separation, as shown in Figure 5. During calcination, PAN domains formed the core while the PVP/stannous chloride mixture formed the shell. Both polymers decomposed upon

heating, while the $SnCl_2$ was oxidized to $SnO_2$, resulting in the formation of hollow $SnO_2$ nanotubes as well as solid fibres, depending on the concentration of PAN (see Figure 5). In another study, Zhang et al. [94] employed a single-needle electrospinning technique using a precursor solution composed of PAN, PVP, and zinc acetate. They reported that phase separation occurred during electrospinning, with PAN forming the core and the PVP/zinc acetate mixture forming the shell. Upon annealing, this core–shell structure led to the formation of hollow ZnO nanotubes. This demonstrates that hollow nanotubes can be produced through the combination of immiscible and incompatible polymers, regardless of the specific salt precursor used. In contrast, Wei et al. [95] successfully fabricated hollow ZnO nanotubes using a single polymer in the presence of a precursor. In this approach, hollow structures were formed due to phase separation that occurred during electrospinning, driven by solvent evaporation. The authors used PVP as the polymer, dissolved in a 1:1 mixture of DMF and ethanol, while zinc acetate dihydrate was dissolved in deionized water. The two solutions were then combined and electrospun. It was observed that during electrospinning, $Zn^{2+}$ ions migrated toward the fiber surface as the solvent rapidly evaporated. This migration led to the formation of hollow nanotubes composed of non-uniform ZnO nanoparticles (15–35 nm) distributed along one-dimensional fibers with diameters ranging from 70 to 170 nm after calcination at 600 °C for 3 h in air. The resulting fibers exhibited a rough and porous surface. This morphology was attributed to the rapid evaporation of ethanol, which caused $Zn^{2+}$ ions to accumulate at the fiber boundary and encapsulate the PVP core.

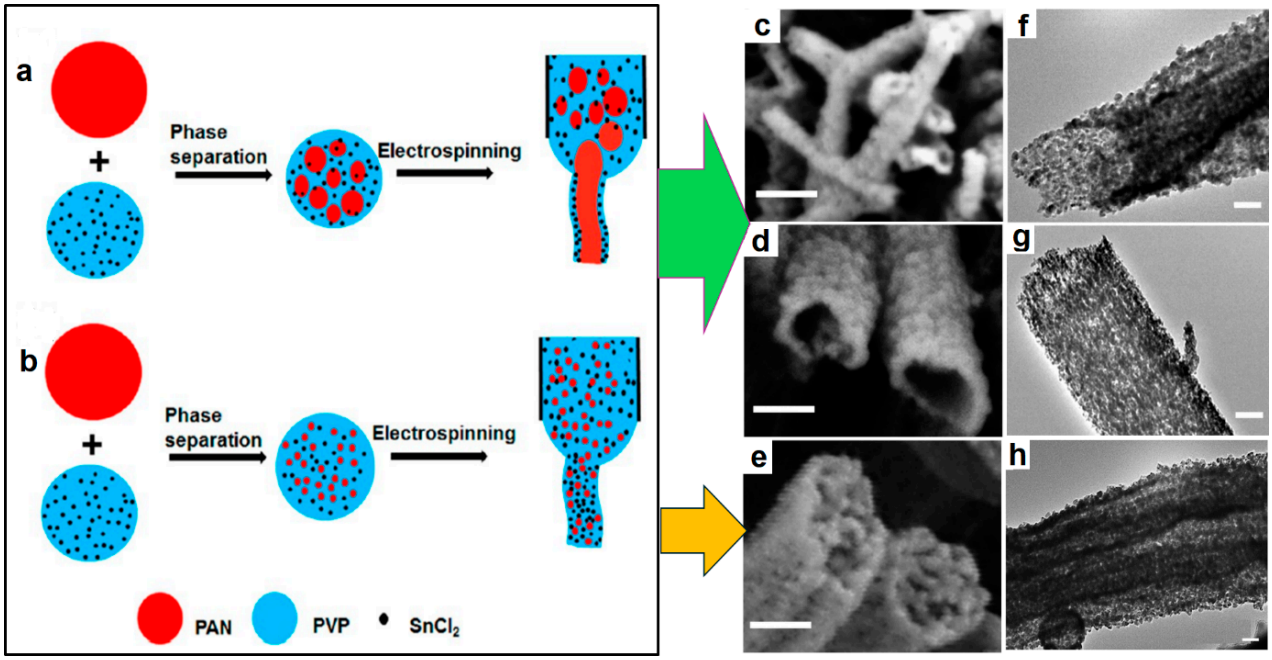


**Figure 5.** Schematic illustration for the formation mechanism of (**a**) hollow and (**b**) solid fibers using electrospinning via the phase separation method. SEM images of (**c**,**d**) hollow nanotubes at low PAN concentration, and (**e**) solid fibers at higher PAN content. TEM images of hollow nanotubes (**f**,**g**) and (**h**) solid fibers. Reproduced with permission from Ab Kadir et al. [93], The Journal of Physical Chemistry C; published by American Chemical Society, 2014.

Post-treatment conditions have been reported to play a critical role in the formation of hollow nanotubes from electrospun nanofibers [96–98]. In particular, the calcination heating rate significantly influences the final fiber morphology. A slow heating rate of 2 °C/min was found to be optimal for producing hollow nanotubes, whereas a higher rate of 10 °C/min resulted in the formation of solid fibers [96]. Although this phenomenon was observed, no

definitive explanation was provided by the authors. It is worth noting that the polymer often used to obtain such morphology is PVP from the $SnO_2$ viewpoint. Su et al. [97] also produced $SnO_2$ nanotubes by electrospinning a solution composed of PVP and $SnCl_2{\cdot}2H_2O$ as salt precursor. They found that heating rates of 2 °C/min produced solid fibers, but 6 °C/min produced well-defined nanotubes, whereas at 10 °C/min, the structure collapsed. The authors attributed the formation of either solid or hollow nanotubes during calcination to two competing effects. The first is fiber shrinkage caused by the thermal decomposition of PVP, which tends to produce solid fibers. The second involves the diffusion of gases generated from PVP decomposition, which escape from the fiber core toward the shell, creating internal pressure that can expand the fiber into a hollow structure. At slow heating rates, the release of gases occurs more rapidly than the decomposition of PVP. This allows gases to diffuse out efficiently, maintaining internal pressure close to the external environment. As a result, shrinkage becomes the dominant effect, leading to the formation of solid fibers. In contrast, at moderate heating rates, the decomposition of PVP accelerates, and the gas diffusion rate becomes slower than the rate of gas generation. This causes gas accumulation inside the fibers, increasing internal pressure. The elevated pressure promotes outward movement of nanoparticles, forming a shell and resulting in hollow nanotubes. In this scenario, expansion due to gas buildup becomes the dominant factor. However, when the heating rate is too high, the rapid decomposition of PVP produces a large volume of gases in a short time. The excessive internal pressure may exceed the mechanical stability of the fibers, leading to structural failure and breakage of the hollow nanotube.

Hwang et al. [99] successfully synthesized hollow ZnO nanotubes by optimizing the annealing temperature. A mixture of PAN and a ZnO precursor was electrospun and subsequently calcined at various temperatures, including 400, 500, 600, and 700 °C. Hollow nanotubes were observed only at annealing temperatures of 500 °C and above. Additionally, it was noted that annealing at 500 °C for one hour produced hollow nanotubes with narrower diameters compared to those annealed for two hours or longer, indicating that extended annealing promotes more complete hollow structure formation, as shown in Figure 6. Elsewhere, n–n junction hybrid hollow nanotubes were synthesized using a single-step method [100]. Metal precursors of ZnO and $SnO_2$ were blended with a polymeric matrix and then processed via electrospinning. The resulting nanofibers were annealed at various temperatures for 2 h, using a constant heating rate of 5 °C/min. It was determined that an annealing temperature of 500 °C was optimal for producing hollow-structured fibers, which exhibited a specific surface area of approximately 37 $m^2/g$ and a pore size distribution ranging from 15 to 39 nm.

**Table 3.** Overview of studies utilizing various polymers as templates for the fabrication of one-dimensional nanostructured materials via electrospinning.

| Polymer and Precursor | Conditions | Post Treatment | Verdict |
| --- | --- | --- | --- |
| PVP<br>$Zn(NO_3)_2{\cdot}6H_2O$ | -Voltage = 19 kV<br>-Feeding rate = 0.05 mL/h<br>-Tip-to-collector distance = 15 cm | Annealed at 550 °C | Polycrystalline ZnO fibers with diameters ranging from 50 to 200 nm were obtained, consisting of multiple layers measuring approximately 10 to 25 nm each [101]. |
| PVA<br>$Co(NO)_2{\cdot}6H_2O$ ≥98% | -Feeding rate = 0.3 μL $h^{-1}$<br>-Voltage = 20 kV | Dried at 60 °C for 3 h, followed by annealing at 600 °C for 3 h | The resulting crystalline $Co_3O_4$ 1D nanostructures retained a spiderweb-like arrangement, with fiber diameters ranging from 100 to 200 nm. These fibers were composed of interconnected nanoparticles measuring approximately 3 to 10 nm, forming a porous structure [102]. |

**Table 3.** *Cont.*

| Polymer and Precursor | Conditions | Post Treatment | Verdict |
| --- | --- | --- | --- |
| PAN/PVP $ZnCl_2/CoCl_2{\cdot}6H_2O$ | -Voltage = 16 kV<br>-Tip-to-collector distance = 15 cm<br>-Feeding rate = 1 mL/h | Heated in air at 400, 500, and 6000 °C for 1.5 h | The one-dimensional fibrous architecture was preserved after calcination. However, annealing at 600 °C led to more pronounced fragmentation of the resulting fibers. The fibers exhibited mesoporosity, with specific surface areas of 6.015, 19.521, and 10.424 $m^2/g$ for samples annealed at 400 °C, 500 °C, and 600 °C, respectively [79]. |
| PVA $(CH_3CO_2)_2Zn$ | -Tip-to-collector distance = 20 cm<br>-Voltage = 10 kV<br>-Feeding rate = 0.5 mL/h | Annealed in air at 400–800 °C for 2 h | Although the fibrous architecture was retained, the fibers consisted of nanograins approximately 20 nm in size. Structural perfection improved with annealing up to 700 °C; however, further temperature increases led to a decline in structural integrity [82]. |
| PVP $SnCl_2{\cdot}2H_2O$ | -Feeding rate = 0.3 mL/h<br>-Voltage = 14 kV<br>-Tip-to-collector distance = 15 cm | Annealed in air at 500 °C for 2 h at different heating rates of 2 °C/min, 6 °C/min, and 10 °C/min | The heating rate influenced the structure of the resulting one-dimensional materials: a rate of 2 °C/min produced solid fibers, and 6 °C/min resulted in the formation of hollow nanotubes. In comparison, a rate of 10 °C/min caused most of the nanotubes to collapse [97]. |
| PVP $SnCl_2{\cdot}2H_2O/PdCl_2$ | -Voltage = 20 kV<br>-Tip-to-collector distance = 10 cm | Annealed at 600 °C for 2 h | Hollow nanotubes of Pd-doped $SnO_2$ nanofiber were attained using single needle electrospinning [83]. |
| PAN $SnO_2$ | -Voltage = 20 kV<br>-Tip-to-collector distance = 10 cm<br>-Feeding rate = 0.5 mL/h | PAN was stabilized at 250 °C for 2 h, followed by calcination at 700 °C for 1 h. | Coating a PAN template with a $SnO_2$ precursor via atomic layer deposition (ALD), followed by calcination, resulted in smooth, wrinkle-free $SnO_2$ nanotubes. This was attributed to the stabilizing effect of PAN during the deposition and thermal treatment processes [84]. |
| PVP $Zn(AC)_2{\cdot}2H_2O$ | -Voltage = 19 kV<br>-Tip-to-collector distance = 20 cm | Annealed at 600 °C for 3 h in air | Solvent evaporation-induced phase separation resulted in the formation of one-dimensional ZnO nanotubes with a surface area of 99.2 $m^2/g$ [95]. |
| PVP $SnCl_4{\cdot}2H_2O/Zn(NO_3)_2{\cdot}6H_2O$ | -Voltage = 20 kV<br>-Tip-to-collector distance = 20 cm<br>-Humidity = 40–50 | Annealed at 600 °C for 3 h in air with a heating rate of 10 °C/min | Porous hollow $SnO_2$ and ZnO nanotubes composed of nanoparticles approximately $10 \pm 5$ nm in size [98]. |
| PVP $SnCl_2{\cdot}2H_2O/Zn(NO_3)_2{\cdot}6H_2O$ | -Voltage = 18 kV<br>-Tip-to-collector distance =15 cm | Annealed at 600 °C for 3 h in air at a heating rate of 1 °C/minute | Smooth fibers were initially obtained before annealing. However, during the annealing process, Sn and Zn ions diffused toward the fiber surface. Continued heating led to the decomposition of the polymer matrix, along with chloride and nitrate ions, facilitating the oxidation of Zn and Sn into nanograins. As the temperature increased, these nanograins grew and reorganized to form hollow nanotubes. The resulting structures were mesoporous, with pore sizes ranging from 2 to 50 nm and a specific surface area of approximately 17 $m^2/g$ [77]. |
| PVP $Zn(CH_3COO)_2{\cdot}2H_2O/$ $SnCl_2{\cdot}2H_2O/AgNO_3$ | -Voltage = 15 kV | Annealed at 600 °C for 2 h | Rough, porous tubular structures were formed, exhibiting an average diameter of about 248 nm and a wall thickness of around 24 nm [103]. |
| PVP $SnCl_2{\cdot}2\ H_2O/AuCl_3{\cdot}HCl{\cdot}4H_2O$ | -Voltage = 15 kV<br>-Feeding rate = 8 µL/min<br>-Tip-to-collector distance = 15 cm | Annealed at 500 °C for 2 h in air at a heating rate of 3 °C/min | Nanotubes with diameters ranging from 60 to 90 nm were decorated with gold nanoparticles via ultraviolet light irradiation, resulting in well-dispersed nanoparticles uniformly distributed along the nanotube surfaces [104]. |

**Table 3.** *Cont.*

| Polymer and Precursor | Conditions | Post Treatment | Verdict |
|---|---|---|---|
| PVP/PS<br>Zn $(CH_3COO)_2 \cdot H_2O$/Co<br>$(CH_3COO)_2 \cdot 4H_2O$/Ni<br>$(CH_3COO)_2 \cdot 4H_2O$ | -Voltage = 20 kV<br>-Tip-to-collector distance = 15 cm<br>-Feeding rate = 0.6 mL/h | Annealed for 2 h at 400 °C with a heating rate of 1 °C/min in air | Salt precursors were mixed with PVP, and the PS was introduced into the system to produce nanotubes after electrospinning and annealing at 400 °C for 2 h, with a surface area reaching ~29 $m^2/g$ [78]. |
| PVP<br>$Zn(NO_3)_2 \cdot 6H_2O/SnCl_2 \cdot 2H_2O$ | - | Annealed at 600 °C for 5 h | Before calcination, smooth fibers with diameters of up to 200 nm were obtained. Following annealing, the fibers developed a wrinkled and rough surface morphology, with an average diameter reduced to approximately 150 nm. The resulting hollow nanotubes exhibited a rough and porous surface, composed of ZnO and $SnO_2$ nanoparticles ranging in size from 5 to 20 nm, and featured wall thicknesses of around 20 nm [105]. |
| PVP<br>$SnCl_2 \cdot 2H_2O/Zn(AC)_2$ | -Voltage = 15 kV<br>-Tip-to-collector distance = 15 cm | Annealed at 600 °C for 3 h at a rate of 2 °C/min | The resulting tubes had a diameter of approximately 800 nm, with a wall thickness of about 100 nm [75]. |

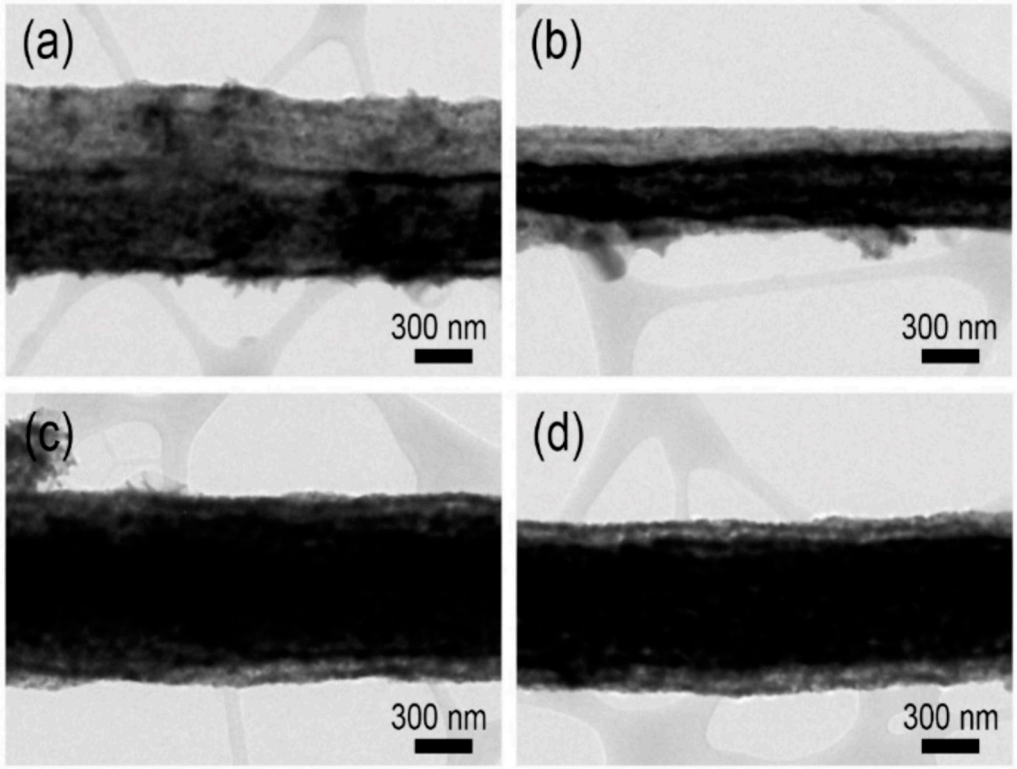


**Figure 6.** TEM images of ZnO resulting from annealing at 500 °C at different times (**a**) 1 h, (**b**) 2 h, (**c**) 3 h, and (**d**) 4 h [99].

### *4.3. Gas Sensing Performance*

The polymer-assisted synthesis methods provide 1D MOS materials with high surface area and abundant active sites, promoting efficient gas adsorption and diffusion [106,107]. This structural optimization translates directly into improved gas sensor performance at the experimental level. Overall, the works reported highlight how the integration of polymers in the fabrication process serves a vital structural and morphological function, enabling the development of MOS nanomaterials with superior sensing properties [108,109].

For instance, Morais et al. [110] reported on the synthesis and gas sensing performance of $WO_3$ nanofibers prepared via the electrospinning method. This approach enabled the

authors to precisely control the morphology, grain size, and porosity of the nanofibers, key factors that contributed to enhanced gas sensing capabilities. The study systematically investigated the sensor response toward $NO_2$, demonstrating notable sensitivity, selectivity, and fast response and recovery times. The researchers emphasized the critical role of the PVP polymer used in the electrospinning precursor solution, which primarily acted as a templating and fiber-forming agent. By modulating the concentration of PVP and molecular weight, the microstructural characteristics of the $WO_3$ fibers could effectively be controlled. Importantly, the PVP was removed after calcination, ensuring that the final sensing material was composed solely of $WO_3$. The unique 1D nanofiber structure achieved through polymer-assisted synthesis provided a high surface area and abundant active sites, promoting efficient gas adsorption and diffusion.

Similarly, Feng et al. [111] used PVP as a templating and fiber-forming agent during the electrospinning process of In-NiO, allowing for the creation of uniform, 1D porous In-NiO nanofibers. After calcination at 500 °C, the PVP was removed entirely, leaving behind p-type In-NiO nanofibers with high surface area and optimized morphology. The obtained nanofibers demonstrated significant sensitivity and selectivity toward methanol gas, along with response and recovery times of 273 and 26 s at an operating temperature of 300 °C. The improved sensor performance was primarily attributed to the intrinsic properties of NiO, combined with the porous nanofiber structure enabled by the polymer-assisted synthesis.

Kgomo et al. [35] reported on a single-step electrospinning method to fabricate mesoporous, belt-like $In_2O_3$ for methane sensing, systematically exploring how annealing temperature influences morphology, surface defects, and textural characteristics. Among the samples tested, the sensor annealed at 550 °C demonstrated exceptional performance: a response factor of 1.1 to 90 ppm of methane at a low operating temperature of 100 °C, with fast response and recovery times of 36 s and 44 s, respectively, as well as good stability, selectivity, and a low detection limit of 0.18 ppm. The enhanced performance is attributed to the mesoporous belt-like morphology composed of small particles (see Figure 7), which provides a high surface area, abundant oxygen vacancies, and numerous active sites, facilitating efficient methane adsorption and desorption.

In another study by Dong et al. [112], the authors presented a polymer-template-assisted electrospinning method, enhanced by solvent evaporation–induced phase separation, to synthesize porous $\alpha$-$Fe_2O_3$ nanofibers for ethanol sensing. In their approach, PVP served both as a structural template and as a carrier for the iron precursor. At the same time, a binary solvent system with differing volatilities was used to drive pore formation during fiber spinning. The phase separation process produced polymer-rich and polymer-lean domains that, upon calcination, yielded an interconnected porous $\alpha$-$Fe_2O_3$ network. Structural analyses confirmed uniform porosity and crystallinity, and the resulting fibers exhibited significantly higher ethanol sensitivity and ultrafast response times compared to non-porous counterparts, owing to their increased surface area and shorter gas diffusion pathways. Further studies are listed in Table 4, whereby the polymer template, synthesis method, resulting morphology and key sensing performance metrics are discussed.

Across these studies in Table 4 and the other studies discussed throughout this review, a clear set of insights emerges on the role and importance of polymer templates in the synthesis of 1D MOS nanomaterials for gas sensing. In all cases, the polymer, most often PVP, functions as both a fiber-forming agent and a sacrificial template that governs the final morphology of the material, porosity, and surface characteristics. By combining polymer templating with electrospinning, continuous, uniform nanofibers, belt-like structures, and nanotubes with high surface area and abundant active sites can be produced. These structural features directly enhance gas–solid interactions by increasing adsorption capacity and enabling faster gas diffusion through the sensing layer. The calcination step not only

crystallizes the MOS phase but also removes the polymer, leaving a pure oxide framework with tailored porosity and optimized grain connectivity. This structural control is essential for translating material-level design into measurable improvements in sensitivity, selectivity, and response/recovery dynamics.

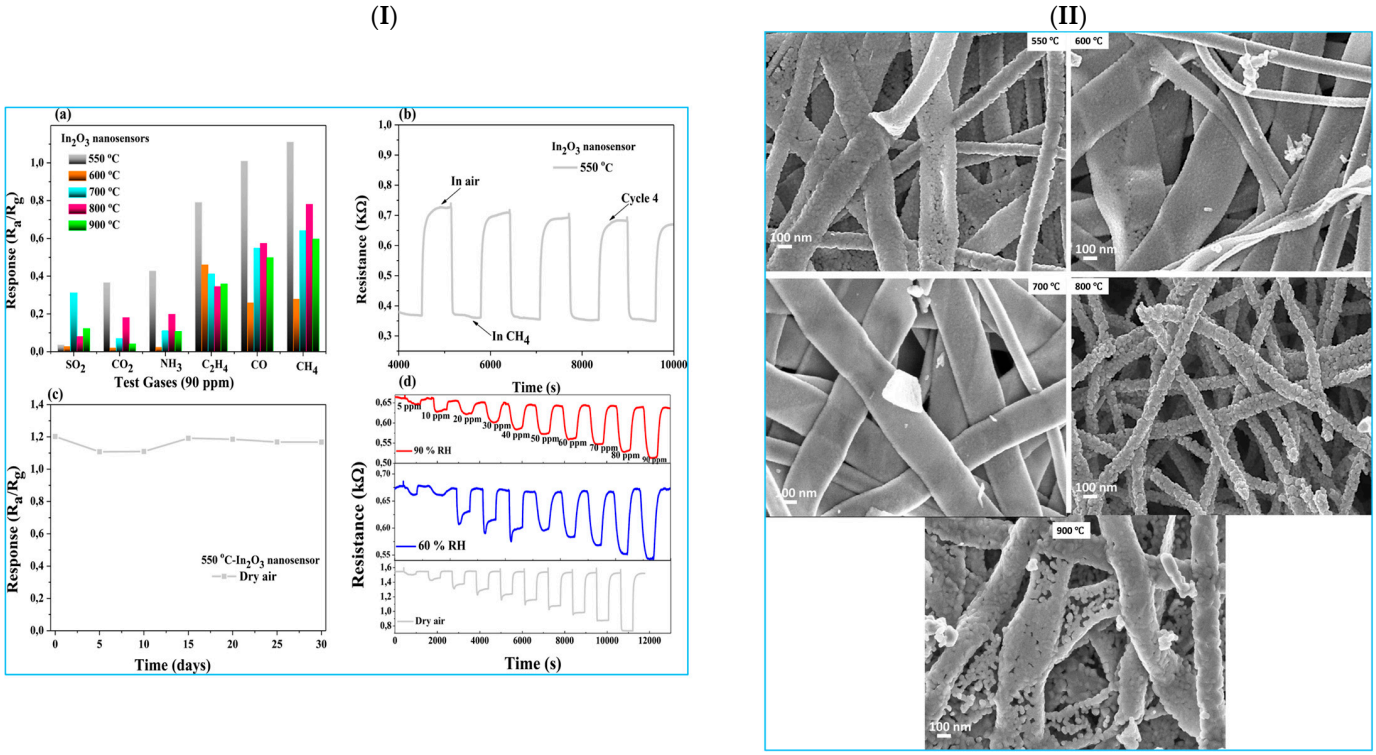


**Figure 7.** (**I**) Gas sensing performance of the $In_2O_3$ belt-like structures obtained through electrospinning showing the (**a**) Selectivity of the fibers, (**b**) response reproducibility curves, and (**c**) 30 days stability measurements, (**d**) resistance curves towards 90 ppm of $CH_4$ in different levels of relative humidity levels (0%, 60% and 90%) and (**II**) FE-SEM images of the $In_2O_3$ belt-like samples at different annealing temperatures. Reproduced with permission from Kgomo et al. [35], Materials Research Bulletin; published by Elsevier, 2023.

**Table 4.** MOS obtained through polymer templating and their gas sensing performance.

| Polymer Template/MOS | Method | Morphology | Gas Sensing Performance | Refs. |
|---|---|---|---|---|
| PVP-$WO_3$ | Electrospinning | Nanofibers | ~ High selectivity towards 0.5 ppm of $NO_2$ at 150 °C. | [110] |
| PVP-In doped NiO | Electrospinning | Nanofibers | ~ Enhanced response to 200 ppm towards methanol at 300 °C. Response and recovery time of 273 s/26 s at 200 ppm. | [111] |
| PVP-$InGaZnO_4$ | RF sputtering coating. | Submicron tubes | ~ High response of 109.5 towards 2 ppm $NO_2$ at 300 °C. | [113] |
| PVP-$\alpha$-$Fe_2O_3$ | Electrospinning | Nanofibers | ~Highly sensitive and ultrafast recovery time of 7 and 5 s towards 1000 ppm ethanol at 340 °C. | [112] |
| AAO-ZnO | Vacuum sucking | Nanowires | ~ 68% sensitivity towards 50 ppm $NH_3$ with response and recovery time of 28 s and 29 s at room temperature. | [114] |

**Table 4.** *Cont.*

| Polymer Template/MOS | Method | Morphology | Gas Sensing Performance | Refs. |
|---|---|---|---|---|
| PVP-$In_2O_3$ | Electrospinning | Belt-like | ~ Response factor of 1.1 to 90 ppm of methane at 100 °C, with response and recovery time of 36 s and 44 s, and LOD of 0.18 ppm. | [35] |
| PAN-ZnO | Vapour Liquid Solid | Nanofibers | ~ Excellent sensitivity and selectivity towards ethanol. ~ The sensitivity for ethanol increased from 2.59 for 10 ppm to 20.23 for 500 ppm. | [115] |
| PVP-$WO_3$ | Electrospinning | Nanofibers | ~ The porous $WO_3$ nanofibers detected 700 ppb of acetone with 3 V bias voltage using photo-activation with a response/recovery time of 33 s/42 s and excellent repeatability. | [116] |
| PVP/$In_2O_3$@$PW_{12}$@$SnO_2$ | Electrospinning | Nanofibers | ~ Response of 22.6 towards 100 ppm ethanol with LOD of 13.9 ppb. | [117] |
| PVP/$LaFeO_3$/$Fe_2O_3$ | Electrospinning | Nanofibers | ~ $LaFeO_3$:$Fe_2O_3$ = 10:1 sensor had a response of 38.46 towards 100 ppm formaldehyde at 120 °C, with response and recovery time of 3 s and 11 s. | [118] |

## 5. Challenges and Prospects

The use of polymer templates in the synthesis of 1D MOS gas sensors presents several challenges and prospects. Among the main challenges are the typically high operating temperatures required for MOS sensors, which result in high power consumption and potential structural degradation, limiting safe and practical applications [29]. Achieving efficient room-temperature sensing remains a major hurdle. Additionally, selectivity is a significant issue, as MOS sensors often struggle to differentiate target gases from interfering ones, complicating reliable detection [2]. Detecting gases at very low concentrations and maintaining sensor stability under variable environmental conditions, such as fluctuations in humidity and temperature, is also challenging to achieve [2]. While polymer templates enable controlled morphology and microstructure design, reproducibly fabricating the ideal pore structure, grain size, and defect density for consistent performance is complex. Furthermore, scaling up from laboratory-scale polymer templating methods like electrospinning to cost-effective, commercial manufacturing is still an ongoing challenge.

Looking ahead, there are several exciting prospects for polymer-templated 1D MOS gas sensors. Advances in polymer chemistry and templating techniques can further enhance control over the microstructure, enabling sensors with higher surface area, optimized porosity, and defect engineering that could operate effectively at or near room temperature, significantly reducing power consumption. Combining metal oxides with conducting polymers, noble metal nanoparticles, or carbon-based materials offers synergistic improvements in sensitivity, selectivity, and response speed [119–122]. Novel synthesis methods such as solvent-induced phase separation and multi-template approaches could produce nanostructures with superior gas diffusion and adsorption properties. The development of flexible, wearable, and miniaturized sensor platforms incorporating polymer-templated MOS structures is a growing trend driven by the need for portable and real-time gas monitoring [65,123]. Additionally, strategies like doping and heterojunction formation

combined with polymer templating open pathways to multi-gas sensing with enhanced specificity. Overall, polymer templates remain a powerful and versatile tool for overcoming current limitations and advancing the design of next-generation, high-performance, energy-efficient, and cost-effective 1D MOS gas sensors.

## 6. Conclusions

In conclusion, polymer templates play a pivotal and active role in the synthesis of 1D MOS nanomaterials for gas sensing applications. Their dual function as fiber-forming agents and sacrificial templates enables precise control over the morphology, porosity, and surface characteristics of the resulting MOS structures. Through polymer-assisted methods such as electrospinning, researchers can reliably fabricate continuous, uniform, and highly porous nanofibers, belts, and nanotubes that exhibit enhanced gas adsorption, accelerated diffusion, and improved gas–solid interactions. The calcination process further refines these materials by crystallizing the MOS phase and removing the polymer, leaving optimized porous frameworks with tailored grain connectivity.

Moreover, polymer templates allow for fine-tuning critical microstructural parameters such as grain size, pore distribution, and defect density that directly influence sensing performance metrics like sensitivity, selectivity, and response/recovery times. Studies across diverse MOS have demonstrated that variations in polymer type, concentration, and processing conditions can be strategically employed to target specific gases with superior sensing dynamics. Therefore, polymer-assisted synthesis is not merely a fabrication convenience but a powerful design tool that enables the engineering of 1D MOS nanostructures with exceptional functional properties. As demand for high-performance, cost-effective gas sensors continues to grow, using polymer templates will remain a central strategy in advancing the next generation of metal oxide-based gas sensor technologies.

**Funding:** The authors would like to acknowledge the University of the Witwatersrand, NRF Thuthuka (TTK230508103666), NRF Postgraduate Scholarships, and DSTI/Mintek NIC for financial support.

**Data Availability Statement:** No new data were created or analyzed in this study.

**Conflicts of Interest:** The authors declare no conflicts of interest or competing financial interests.

## References

1. Saxena, P.; Shukla, P. A review on recent developments and advances in environmental gas sensors to monitor toxic gas pollutants. *Environ. Prog. Sustain. Energy* **2023**, *42*, e14126. [CrossRef]
2. Goel, N.; Kunal, K.; Kushwaha, A.; Kumar, M. Metal oxide semiconductors for gas sensing. *Eng. Rep.* **2023**, *5*, e12604. [CrossRef]
3. Dey, A. Semiconductor metal oxide gas sensors: A review. *Mater. Sci. Eng. B* **2018**, *229*, 206–217. [CrossRef]
4. Korotcenkov, G. Current trends in nanomaterials for metal oxide-based conductometric gas sensors: Advantages and limitations. part 1: 1D and 2D nanostructures. *Nanomaterials* **2020**, *10*, 1392. [CrossRef]
5. Saleh, T.A. Nanomaterials: Classification, properties, and environmental toxicities. *Environ. Technol. Innov.* **2020**, *20*, 101067. [CrossRef]
6. Martín, J.; Maiz, J.; Sacristan, J.; Mijangos, C. Tailored polymer-based nanorods and nanotubes by" template synthesis": From preparation to applications. *Polymer* **2012**, *53*, 1149–1166. [CrossRef]
7. Lu, Z.; Zhou, Q.; Wang, C.; Wei, Z.; Xu, L.; Gui, Y. Electrospun ZnO–$SnO_2$ composite nanofibers and enhanced sensing properties to $SF_6$ decomposition byproduct $H_2S$. *Front. Chem.* **2018**, *6*, 540. [CrossRef] [PubMed]
8. Zhao, Y.; He, X.; Li, J.; Gao, X.; Jia, J. Porous CuO/$SnO_2$ composite nanofibers fabricated by electrospinning and their $H_2S$ sensing properties. *Sens. Actuators B Chem.* **2012**, *165*, 82–87. [CrossRef]
9. Zhou, Q.; Chen, W.; Peng, S.; Zeng, W. Hydrothermal synthesis and acetylene sensing properties of variety low dimensional zinc oxide nanostructures. *Sci. World J.* **2014**, *2014*, 489170. [CrossRef]
10. Kaur, N.; Singh, M.; Comini, E. One-dimensional nanostructured oxide chemoresistive sensors. *Langmuir* **2020**, *36*, 6326–6344. [CrossRef]

11. Yang, B.; Myung, N.V.; Tran, T. 1D metal oxide semiconductor materials for chemiresistive gas sensors: A review. *Adv. Electron. Mater.* **2021**, *7*, 2100271. [CrossRef]
12. Hontañón, E.; Vallejos, S. One-Dimensional Metal Oxide Nanostructures for Chemical. In *21st Century Nanostructured Materials: Physics, Chemistry, Classification, and Emerging Applications in Industry, Biomedicine, and Agriculture*; Intechopen: London, UK, 2022; Volume 927.11, p. 151.
13. Tong, Y.; Liu, Y.; Dong, L.; Zhao, D.; Zhang, J.; Lu, Y.; Shen, D.; Fan, X. Growth of ZnO nanostructures with different morphologies by using hydrothermal technique. *J. Phys. Chem. B* **2006**, *110*, 20263–20267. [CrossRef]
14. Shen, G.; Tandio, A.R.; Hong, F.C. Hydrothermally synthesized ultrathin zinc oxide nanowires based field-effect transistors. *Thin Solid Film.* **2016**, *618*, 100–106. [CrossRef]
15. Zhou, Y.; Liu, Q.; Yang, C.; Zhao, Z. Interfacial micro-structure and properties of $TiO_2/SnO_2$ heterostructures with rutile phase: A DFT calculation investigation. *Appl. Surf. Sci.* **2018**, *451*, 258–271. [CrossRef]
16. Sharma, D.K.; Shukla, S.; Sharma, K.K.; Kumar, V. A review on ZnO: Fundamental properties and applications. *Mater. Today Proc.* **2022**, *49*, 3028–3035. [CrossRef]
17. Jagadale, S.B.; Patil, V.L.; Vanalakar, S.A.; Patil, P.S.; Deshmukh, H.P. Preparation, characterization of 1D ZnO nanorods and their gas sensing properties. *Ceram. Int.* **2018**, *44*, 3333–3340. [CrossRef]
18. Tshabalala, Z.P.; Mokoena, T.P.; Jozela, M.; Tshilongo, J.; Hillie, T.K.; Swart, H.C.; Motaung, D.E. $TiO_2$ nanowires for humidity-stable gas sensors for toluene and xylene. *ACS Appl. Nano Mater.* **2020**, *4*, 702–716. [CrossRef]
19. Samykano, M. Progress in one-dimensional nanostructures. *Mater. Charact.* **2021**, *179*, 111373. [CrossRef]
20. Cai, Y.H.; Ma, S.Y.; Wei, J.S. Highly sensitive triethylamine sensor with ppb level detection limit based on SnSe nanofibers. *Ceram. Int.* **2023**, *49*, 15333–15340. [CrossRef]
21. Yin, M.; Liu, S. Preparation of ZnO hollow spheres with different surface roughness and their enhanced gas sensing property. *Sens. Actuators B Chem.* **2014**, *197*, 58–65. [CrossRef]
22. Shingange, K. The exploration of lanthanum Based Complexes Oxides: Preparation, Characterization and Gas Sensing Properties. Ph.D. Thesis, University of the Free State, Bloemfontein, South Africa, 2019.
23. Yuan, Z.; Zhang, H.; Li, J.; Meng, F.; Yang, Z.; Zhang, H. Ag nanoparticle-modified ZnO–$In_2O_3$ nanocomposites for low-temperature rapid detection hydrogen gas sensors. *IEEE Trans. Instrum. Meas.* **2023**, *72*, 1–12. [CrossRef]
24. Shingange, K.; Swart, H.C.; Mhlongo, G.H. $H_2S$ detection capabilities with fibrous-like La-doped ZnO nanostructures: A comparative study on the combined effects of La-doping and post-annealing. *J. Alloys Compd.* **2019**, *797*, 284–301. [CrossRef]
25. Quitério, P.; Apolinário, A.; Sousa, C.T.; Costa, J.D.; Ventura, J.; Araújo, J.P. The cyclic nature of porosity in anodic $TiO_2$ nanotube arrays. *J. Mater. Chem. A* **2015**, *3*, 3692–3698. [CrossRef]
26. Yu, H.; Wang, J.; Xia, C.; Yan, X.; Cheng, P. Template-free hydrothermal synthesis of Flower-like hierarchical zinc oxide nanostructures. *Optik* **2018**, *168*, 778–783. [CrossRef]
27. Moumen, A.; Kaur, N.; Poli, N.; Zappa, D.; Comini, E. One dimensional ZnO nanostructures: Growth and chemical sensing performances. *Nanomaterials* **2020**, *10*, 1940. [CrossRef]
28. Galdámez-Martinez, A.; Santana, G.; Güell, F.; Martínez-Alanis, P.R.; Dutt, A. Photoluminescence of ZnO nanowires: A review. *Nanomaterials* **2020**, *10*, 857. [CrossRef]
29. Nadargi, D.Y.; Umar, A.; Nadargi, J.D.; Lokare, S.A.; Akbar, S.; Mulla, I.S.; Suryavanshi, S.S.; Bhandari, N.L.; Chaskar, M.G. Gas sensors and factors influencing sensing mechanism with a special focus on MOS sensors. *J. Mater. Sci.* **2023**, *58*, 559–582. [CrossRef]
30. Shingange, K.; Mhlongo, G.H. Correlating Luminescence Characteristics to Gas-Sensing Performance of Metal Oxides Based Heterostructures. In *Luminescent Nanomaterials*; Jenny Stanford Publishing: Singapore, 2022; pp. 163–178.
31. Ye, K.; Li, K.; Lu, Y.; Guo, Z.; Ni, N.; Liu, H.; Huang, Y.; Ji, H.; Wang, P. An overview of advanced methods for the characterization of oxygen vacancies in materials. *TrAC Trends Anal. Chem.* **2019**, *116*, 102–108. [CrossRef]
32. Mhlongo, G.H.; Shingange, K.; Tshabalala, Z.P.; Dhonge, B.P.; Mahmoud, F.A.; Mwakikunga, B.W.; Motaung, D.E. Room temperature ferromagnetism and gas sensing in ZnO nanostructures: Influence of intrinsic defects and Mn, Co, Cu doping. *Appl. Surf. Sci.* **2016**, *390*, 804–815. [CrossRef]
33. Benghanem, M.; Ahmad, Z.; Shkir, M.; Alshahrani, T. Growth of $Y^3$ doped $CeO_2$ films and their structural, optical, photoluminescence, and gas sensing studies. *J. Sol-Gel Sci. Technol.* **2025**, *115*, 1567–1579. [CrossRef]
34. Tyagi, S.; Kumar, A.; Kumar, A.; Gautam, Y.K.; Kumar, V.; Kumar, Y.; Singh, B.P. Enhancement in the sensitivity and selectivity of Cu functionalized $MoS_2$ nanoworm thin films for nitrogen dioxide gas sensor. *Mater. Res. Bull.* **2022**, *150*, 111784. [CrossRef]
35. Kgomo, M.B.; Shingange, K.; Nemufulwi, M.I.; Swart, H.C.; Mhlongo, G.H. Belt-like $In_2O_3$ based sensor for methane detection: Influence of morphological, surface defects and textural behavior. *Mater. Res. Bull.* **2023**, *158*, 112076. [CrossRef]
36. Shingange, K.; Mhlongo, G.H.; Motaung, D.E.; Ntwaeaborwa, O.M. Tailoring the sensing properties of microwave-assisted grown ZnO nanorods: Effect of irradiation time on luminescence and magnetic behaviour. *J. Alloys Compd.* **2016**, *657*, 917–926. [CrossRef]

37. Yu, S.; Dong, J.; Wang, H.; Li, S.; Zhu, H.; Yang, T. High-performance trimethylamine gas sensors based on defect-engineering MOF-derived ZnO nanoclusters with tunable surface oxygen vacancies. *J. Mater. Chem. A* **2022**, *10*, 25453–25462. [CrossRef]
38. Sun, K.; Zhan, G.; Zhang, L.; Wang, Z.; Lin, S. Highly sensitive $NO_2$ gas sensor based on ZnO nanoarray modulated by oxygen vacancy with Ce doping. *Sens. Actuators B Chem.* **2023**, *379*, 133294. [CrossRef]
39. Meng, F.; Guo, X. Tuning the oxygen defects and Fermi levels via $In^{3+}$ doping in $SnO_2$-$In_2O_3$ nanocomposite for efficient CO detection. *Sens. Actuators B Chem.* **2022**, *357*, 131412. [CrossRef]
40. Kim, W.; Choi, M.; Yong, K. Generation of oxygen vacancies in ZnO nanorods/films and their effects on gas sensing properties. *Sens. Actuators B Chem.* **2015**, *209*, 989–996. [CrossRef]
41. Yang, H.; Zhao, M.; Li, L.; Zhang, L. ZnO nanorods with doubly positive oxygen vacancies for efficient xylene sensing. *ACS Appl. Nano Mater.* **2022**, *5*, 3512–3520. [CrossRef]
42. Kwon, Y.J.; Kim, H.W.; Ko, W.C.; Choi, H.; Ko, Y.; Jeong, Y.K. Laser-engineered oxygen vacancies for improving the $NO_2$ sensing performance of $SnO_2$ nanowires. *J. Mater. Chem. A* **2019**, *7*, 27205–27211. [CrossRef]
43. Shingange, K.; Swart, H.; Mhlongo, G.H. Ultrafast detection of low acetone concentration displayed by Au-loaded $LaFeO_3$ nanobelts owing to synergetic effects of porous 1D morphology and catalytic activity of Au nanoparticles. *ACS Omega* **2019**, *4*, 19018–19029. [CrossRef]
44. Fan, F.; Zhang, J.; Li, J.; Zhang, N.; Hong, R.; Deng, X.; Tang, P.; Li, D. Hydrogen sensing properties of Pt-Au bimetallic nanoparticles loaded on ZnO nanorods. *Sens. Actuators B Chem.* **2017**, *241*, 895–903. [CrossRef]
45. Sun, P.; Yu, Y.; Xu, J.; Sun, Y.; Ma, J.; Lu, G. One-step synthesis and gas sensing characteristics of hierarchical $SnO_2$ nanorods modified by Pd loading. *Sens. Actuators B Chem.* **2011**, *160*, 244–250. [CrossRef]
46. Shingange, K.; Tshabalala, Z.P.; Ntwaeaborwa, O.M.; Motaung, D.E.; Mhlongo, G.H. Highly selective $NH_3$ gas sensor based on Au loaded ZnO nanostructures prepared using microwave-assisted method. *J. Colloid Interface Sci.* **2016**, *479*, 127–138. [CrossRef] [PubMed]
47. Domènech-Gil, G.; Barth, S.; Samà, J.; Pellegrino, P.; Gràcia, I.; Cané, C.; Romano-Rodriguez, A. Gas sensors based on individual indium oxide nanowire. *Sens. Actuators B Chem.* **2017**, *238*, 447–454. [CrossRef]
48. Huang, Y.; Yu, Y.; Yu, Y.; Zhang, B. Oxygen vacancy engineering in photocatalysis. *Sol. RRL* **2020**, *4*, 2000037. [CrossRef]
49. Zhao, R.; Wang, Z.; Yang, Y.; Xing, X.; Zou, T.; Wang, Z.; Hong, P.; Peng, S.; Wang, Y. Pd-functionalized $SnO_2$ nanofibers prepared by shaddock peels as bio-templates for high gas sensing performance toward butane. *Nanomaterials* **2018**, *9*, 13. [CrossRef]
50. Raza, M.H.; Di Chio, R.; Movlaee, K.; Amsalem, P.; Koch, N.; Barsan, N.; Neri, G.; Pinna, N. Role of heterojunctions of core–shell heterostructures in gas sensing. *ACS Appl. Mater. Interfaces* **2022**, *14*, 22041–22052. [CrossRef]
51. Chaiyo, P.; Makhachan, C.; Nutariya, J.; Thiabgoh, O.; Sumran, S.; Pukird, S. Electrical and Sensitivity Properties of ZnO/$TiO_2$ Heterojunction Nanocomposites for Ammonia Gas Sensor. *J. Phys. Conf. Ser.* **2019**, *1259*, 012005.
52. Pura, J.L. Optical and electrical properties of low-dimensional crystalline materials: A review. *Crystals* **2023**, *13*, 108. [CrossRef]
53. Musa, I.; Qamhieh, N. Study of optical energy gap and quantum confinment effects in Zinc Oxide nanoparticles and nanorods. *Dig. J. Nanomater. Biostruct* **2019**, *14*, 119–125.
54. Kamarulzaman, N.; Abdul Aziz, N.D.; Kasim, M.F.; Chayed, N.F.; Yahaya Subban, R.H.; Badar, N. Anomalies in wide band gap $SnO_2$ nanostructures. *J. Solid State Chem.* **2019**, *277*, 271–280. [CrossRef]
55. Wang, Y.; Guo, S.; Xin, X.; Zhang, Y.; Wang, B.; Tang, S.; Li, X. Effective interface contact on the hierarchical 1D/2D CoO/NiCo-LDH heterojunction for boosting photocatalytic hydrogen evolution. *Appl. Surf. Sci.* **2021**, *549*, 149108. [CrossRef]
56. Machín, A.; Fontánez, K.; Arango, J.C.; Ortiz, D.; De León, J.; Pinilla, S.; Nicolosi, V.; Petrescu, F.I.; Morant, C.; Márquez, F. One-dimensional (1D) nanostructured materials for energy applications. *Materials* **2021**, *14*, 2609. [CrossRef]
57. Dhall, S.; Mehta, B.R.; Tyagi, A.K.; Sood, K. A review on environmental gas sensors: Materials and technologies. *Sens. Int.* **2021**, *2*, 100116. [CrossRef]
58. Pourhakkak, P.; Taghizadeh, A.; Taghizadeh, M.; Ghaedi, M.; Haghdoust, S. Chapter 1-Fundamentals of adsorption technology. *Interface Sci. Technol.* **2021**, *33*, 1–70.
59. Budinski-Petković, L.; Tošić, T. Adsorption, desorption and diffusion of extended objects on a square lattice. *Phys. A Stat. Mech. Its Appl.* **2003**, *329*, 350–356. [CrossRef]
60. Moseley, P.T. Materials selection for semiconductor gas sensors. *Sens. Actuators B Chem.* **1992**, *6*, 149–156. [CrossRef]
61. Padvi, M.N.; Moholkar, A.V.; Prasad, S.R.; Prasad, N.R. A critical review on design and development of gas sensing materials. *Eng. Sci.* **2021**, *15*, 20–37. [CrossRef]
62. Park, J.Y.; Choi, S.; Kim, S.S. A synthesis and sensing application of hollow ZnO nanofibers with uniform wall thicknessesgrown using polymer templates. *Nanotechnology* **2010**, *21*, 475601. [CrossRef] [PubMed]
63. Carrow, J.K.; Kerativitayanan, P.; Jaiswal, M.K.; Lokhande, G.; Gaharwar, A.K. Polymers for bioprinting. In *Essentials of 3D Biofabrication and Translation*; Elsevier: Amsterdam, The Netherlands, 2015; pp. 229–248.

64. Tamayol, A.; Najafabadi, A.H.; Aliakbarian, B.; Arab-Tehrany, E.; Akbari, M.; Annabi, N.; Juncker, D.; Khademhosseini, A. Hydrogel templates for rapid manufacturing of bioactive fibers and 3D constructs. *Adv. Healthc. Mater.* **2015**, *4*, 2146–2153. [CrossRef]
65. Hossain, M.K.; Drmosh, Q.A. Polymer-Templated Durable and Hydrophobic Nanostructures for Hydrogen Gas Sensing Applications. *Polymers* **2021**, *13*, 4470. [CrossRef]
66. Blaszczyk-Lezak, I.; Maiz, J.; Sacristán, J.; Mijangos, C. Monitoring the thermal elimination of infiltrated polymer from AAO templates: An exhaustive characterization after polymer extraction. *Ind. Eng. Chem. Res.* **2011**, *50*, 10883–10888. [CrossRef]
67. Omotosho, K.; Tran, J.; Shevchenko, E.V.; Berman, D. Polymer infiltration synthesis of inorganic nanoporous coatings: Does polymer template affect their properties? *Surf. Coat. Technol.* **2023**, *452*, 129107. [CrossRef]
68. Gong, B.; Peng, Q.; Jur, J.S.; Devine, C.K.; Lee, K.; Parsons, G.N. Sequential vapor infiltration of metal oxides into sacrificial polyester fibers: Shape replication and controlled porosity of microporous/mesoporous oxide monoliths. *Chem. Mater.* **2011**, *23*, 3476–3485. [CrossRef]
69. Albayati, A.H.; Al-ani, A.F.; Mohammed, A.M.; Al-Kheetan, M.J.; Moudhafar, M.M.; Jweihan, Y.S. Understanding the effectiveness of elastomeric and plastomeric polymers on the high-temperature performance of asphalt binders. *Innov. Infrastruct. Solut.* **2025**, *10*, 388. [CrossRef]
70. Wu, K.; Guo, X.; Feng, J.; Yang, X.; Li, F.; Wang, X.; Guo, H. Novel Zwitterionic Hydrogels with High and Tunable Toughness for Anti-Fouling Application. *Gels* **2025**, *11*, 587. [CrossRef] [PubMed]
71. Sionkowska, A. Current research on the blends of natural and synthetic polymers as new biomaterials: Review. *Prog. Polym. Sci.* **2011**, *36*, 1254–1276. [CrossRef]
72. Satchanska, G.; Davidova, S.; Petrov, P.D. Natural and synthetic polymers for biomedical and environmental applications. *Polymers* **2024**, *16*, 1159. [CrossRef]
73. Luo, Y.; Hong, Y.; Shen, L.; Wu, F.; Lin, X. Multifunctional role of polyvinylpyrrolidone in pharmaceutical formulations. *AAPS PharmSciTech* **2021**, *22*, 34. [CrossRef]
74. Senthil, T.; Anandhan, S. Structure–property relationship of sol–gel electrospun ZnO nanofibers developed for ammonia gas sensing. *J. Colloid Interface Sci.* **2014**, *432*, 285–296. [CrossRef]
75. Li, Y.; Zhang, H.; Zhang, X.; Wei, L.; Zhang, Y.; Hai, G.; Sun, Y. Enhanced acetone sensing performance based on hollow coral-like $SnO_2$–ZnO composite nanofibers. *J. Mater. Sci. Mater. Electron.* **2019**, *30*, 15734–15743. [CrossRef]
76. Wei, S.; Zhang, Y.; Zhou, M. Toluene sensing properties of $SnO_2$–ZnO hollow nanofibers fabricated from single capillary electrospinning. *Solid State Commun.* **2011**, *151*, 895–899. [CrossRef]
77. Tang, W.; Wang, J.; Yao, P.; Li, X. Hollow hierarchical $SnO_2$-ZnO composite nanofibers with heterostructure based on electrospinning method for detecting methanol. *Sens. Actuators B Chem.* **2014**, *192*, 543–549. [CrossRef]
78. Alali, K.T.; Liu, T.; Liu, J.; Liu, Q.; Fertassi, M.A.; Li, Z.; Wang, J. Preparation and characterization of ZnO/$CoNiO_2$ hollow nanofibers by electrospinning method with enhanced gas sensing properties. *J. Alloys Compd.* **2017**, *702*, 20–30. [CrossRef]
79. Liming, J.; Xinmei, L.; Rui, Y.; Zhiqi, Y. Effect of calcination temperature on the structure and gas sensing properties of electrospinning ZnO / $Co_3O_4$ nanocomposite fibers. *Inorg. Chem. Commun.* **2025**, *179*, 114719. [CrossRef]
80. Park, J.Y.; Asokan, K.; Choi, S.; Kim, S.S. Growth kinetics of nanograins in $SnO_2$ fibers and size dependent sensing properties. *Sens. Actuators B Chem.* **2011**, *152*, 254–260. [CrossRef]
81. Choi, S.; Park, J.Y.; Kim, S.S. Dependence of gas sensing properties in ZnO nanofibers on size and crystallinity of nanograins. *J. Mater. Res.* **2011**, *26*, 1662–1665. [CrossRef]
82. Katoch, A.; Sun, G.; Choi, S.; Byun, J.; Kim, S.S. Competitive influence of grain size and crystallinity on gas sensing performances of ZnO nanofibers. *Sens. Actuators B Chem.* **2013**, *185*, 411–416. [CrossRef]
83. Choi, J.; Hwang, I.; Kim, S.; Park, J.; Park, S.; Jeong, U.; Kang, Y.C.; Lee, J. Design of selective gas sensors using electrospun Pd-doped $SnO_2$ hollow nanofibers. *Sens. Actuators B Chem.* **2010**, *150*, 191–199. [CrossRef]
84. Kim, W.; Lee, B.; Kim, D.; Kim, H.; Yu, W.; Hong, S. $SnO_2$ nanotubes fabricated using electrospinning and atomic layer deposition and their gassensing performance. *Nanotechnology* **2010**, *21*, 245605. [CrossRef]
85. Cho, N.G.; Yang, D.J.; Jin, M.; Kim, H.; Tuller, H.L.; Kim, I. Highly sensitive $SnO_2$ hollow nanofiber-based $NO_2$ gas sensors. *Sens. Actuators B Chem.* **2011**, *160*, 1468–1472. [CrossRef]
86. Han, C.; Li, X.; Shao, C.; Li, X.; Ma, J.; Zhang, X.; Liu, Y. Composition-controllable p-CuO/n-ZnO hollow nanofibers for high-performance $H_2S$ detection. *Sens. Actuators B Chem.* **2019**, *285*, 495–503. [CrossRef]
87. Li, W.; Ma, S.; Li, Y.; Yang, G.; Mao, Y.; Luo, J.; Gengzang, D.; Xu, X.; Yan, S. Enhanced ethanol sensing performance of hollow ZnO–$SnO_2$ core–shell nanofibers. *Sens. Actuators B Chem.* **2015**, *211*, 392–402. [CrossRef]
88. Tian, L.; Sun, Y.; Huang, H.; Guo, X.; Qiao, Z.; Meng, J.; Zhong, C. Porous ZIF-8 Thin Layer Coating on ZnO Hollow Nanofibers for Enhanced Acetone Sensing. *ChemistrySelect* **2020**, *5*, 2401–2407. [CrossRef]
89. Wang, Y.; Wang, X.; Qi, B.; Cheng, J.; Wang, X.; Shang, Y.; Jia, J. Design of $SnO_2$/ZnO@ ZIF-8 Hydrophobic Nanofibers for Improved $H_2S$ Gas Sensing. *ChemistrySelect* **2021**, *6*, 5488–5495. [CrossRef]

90. Lee, J.; Lee, H.; Bae, T.; Cho, D.; Choi, M.; Bae, G.; Shim, Y.; Jeon, S. 3D ZnO/ZIF-8 Hierarchical Nanostructure for Sensitive and Selective $NO_2$ Sensing at Room Temperature. *Small Struct.* **2024**, *5*, 2300503. [CrossRef]
91. Reddy, C.S.; Murali, G.; Reddy, A.S.; Park, S.; In, I. GO incorporated $SnO_2$ nanotubes as fast response sensors for ethanol vapor in different atmospheres. *J. Alloys Compd.* **2020**, *813*, 152251. [CrossRef]
92. Cao, J.; Zhang, T.; Li, F.; Yang, H.; Liu, S. Enhanced ethanol sensing of $SnO_2$ hollow micro/nanofibers fabricated by coaxial electrospinning. *New J. Chem.* **2013**, *37*, 2031–2036. [CrossRef]
93. Ab Kadir, R.; Li, Z.; Sadek, A.Z.; Abdul Rani, R.; Zoolfakar, A.S.; Field, M.R.; Ou, J.Z.; Chrimes, A.F.; Kalantar-zadeh, K. Electrospun granular hollow $SnO_2$ nanofibers hydrogen gas sensors operating at low temperatures. *J. Phys. Chem. C* **2014**, *118*, 3129–3139. [CrossRef]
94. Zhang, Z.; Li, X.; Wang, C.; Wei, L.; Liu, Y.; Shao, C. ZnO hollow nanofibers: Fabrication from facile single capillary electrospinning and applications in gas sensors. *J. Phys. Chem. C* **2009**, *113*, 19397–19403. [CrossRef]
95. Wei, S.; Zhou, M.; Du, W. Improved acetone sensing properties of ZnO hollow nanofibers by single capillary electrospinning. *Sens. Actuators B Chem.* **2011**, *160*, 753–759. [CrossRef]
96. Wang, L.; Luo, X.; Zheng, X.; Wang, R.; Zhang, T. Direct annealing of electrospun synthesized high-performance porous $SnO_2$ hollow nanofibers for gas sensors. *RSC Adv.* **2013**, *3*, 9723–9728. [CrossRef]
97. Su, P.; Li, W.; Zhang, J.; Xie, X. Chemiresistive gas sensor based on electrospun hollow $SnO_2$ nanotubes for detecting NO at the ppb level. *Vacuum* **2022**, *199*, 110961. [CrossRef]
98. Guo, J.; Li, W.; Zhao, X.; Hu, H.; Wang, M.; Luo, Y.; Xie, D.; Zhang, Y.; Zhu, H. Highly sensitive, selective, flexible and scalable room-temperature $NO_2$ gas sensor based on hollow $SnO_2$/ZnO nanofibers. *Molecules* **2021**, *26*, 6475. [CrossRef]
99. Hwang, S.; Kim, Y.K.; Hong, S.H.; Lim, S.K. Cu/CuO@ ZnO hollow nanofiber gas sensor: Effect of hollow nanofiber structure and P–N junction on operating temperature and sensitivity. *Sensors* **2019**, *19*, 3151. [CrossRef] [PubMed]
100. Bai, S.; Fu, H.; Zhao, Y.; Tian, K.; Luo, R.; Li, D.; Chen, A. On the construction of hollow nanofibers of ZnO-$SnO_2$ heterojunctions to enhance the NO2 sensing properties. *Sens. Actuators B Chem.* **2018**, *266*, 692–702. [CrossRef]
101. Hsu, K.; Fang, T.; Chen, S.; Kuo, E. Gas sensitivity and sensing mechanism studies on ZnO/$La_{0.8}Sr_{0.2}Co_{0.5}Ni_{0.5}O_3$ heterojunction structure. *Ceram. Int.* **2019**, *45*, 8744–8749. [CrossRef]
102. Le, D.T.T.; Tuan, V.A.; Tonezzer, M.; Hung, C.M.; Hoa, N.D. An electrospinning deposited cobalt oxide nanofiber gas sensing device: Selective enhancement as a thermal electronic nose. *RSC Adv.* **2025**, *15*, 15293–15301. [CrossRef] [PubMed]
103. Ma, L.; Ma, S.Y.; Kang, H.; Shen, X.F.; Wang, T.T.; Jiang, X.H.; Chen, Q. Preparation of Ag-doped ZnO-$SnO_2$ hollow nanofibers with an enhanced ethanol sensing performance by electrospinning. *Mater. Lett.* **2017**, *209*, 188–192. [CrossRef]
104. Li, J.; Wang, L.; Cheng, X.; Luo, D.; Huang, B.; Sun, S.; Li, X.; Yang, Z. Low-temperature and high-sensitivity Au-decorated thin-walled $SnO_2$ nanotubes sensor for ethanol detection. *Mater. Today Commun.* **2023**, *37*, 107217. [CrossRef]
105. Wan, G.X.; Ma, S.Y.; Sun, X.W.; Sun, A.M.; Li, X.B.; Luo, J.; Li, W.Q.; Wang, C.Y. Synthesis of wrinkled and porous ZnO–$SnO_2$ hollow nanofibers and their gas sensing properties. *Mater. Lett.* **2015**, *145*, 48–51. [CrossRef]
106. Ezhilan, M.; JBB, A.J.; Babu, K.J.; Rayappan, J.B.B. Hierarchically connected electrospun $WO_3$ nanowires–an acetaldehyde sensor. *J. Alloys Compd.* **2021**, *863*, 158407. [CrossRef]
107. Khalil, A.; Kim, J.J.; Tuller, H.L.; Rutledge, G.C.; Hashaikeh, R. Gas sensing behavior of electrospun nickel oxide nanofibers: Effect of morphology and microstructure. *Sens. Actuators B Chem.* **2016**, *227*, 54–64. [CrossRef]
108. Cao, J.; Zhang, N.; Wang, S.; Chen, C.; Zhang, H. Researching the crystal phase effect on gas sensing performance in $In_2O_3$ nanofibers. *Sens. Actuators B Chem.* **2020**, *305*, 127475. [CrossRef]
109. Pang, Z.; Yang, Z.; Chen, Y.; Zhang, J.; Wang, Q.; Huang, F.; Wei, Q. A room temperature ammonia gas sensor based on cellulose/$TiO_2$/PANI composite nanofibers. *Colloids Surf. A Physicochem. Eng. Asp.* **2016**, *494*, 248–255. [CrossRef]
110. Morais, P.V.; Suman, P.H.; Silva, R.A.; Orlandi, M.O. High gas sensor performance of $WO_3$ nanofibers prepared by electrospinning. *J. Alloys Compd.* **2021**, *864*, 158745. [CrossRef]
111. Feng, C.; Kou, X.; Chen, B.; Qian, G.; Sun, Y.; Lu, G. One-pot synthesis of In doped NiO nanofibers and their gas sensing properties. *Sens. Actuators B Chem.* **2017**, *253*, 584–591. [CrossRef]
112. Dong, S.; Yan, S.; Gao, W.; Liu, G.; Hao, H. A phase separation route to synthesize α-$Fe_2O_3$ porous nanofibers via electrospinning for ultrafast ethanol Sensing. *J. Electron. Mater.* **2018**, *47*, 3934–3941. [CrossRef]
113. Cho, N.G.; Kim, I. $NO_2$ gas sensing properties of amorphous $InGaZnO_4$ submicron-tubes prepared by polymeric fiber templating route. *Sens. Actuators B Chem.* **2011**, *160*, 499–504. [CrossRef]
114. Kumar, N.; Srivastava, A.K.; Nath, R.; Gupta, B.K.; Varma, G.D. Probing the highly efficient room temperature ammonia gas sensing properties of a luminescent ZnO nanowire array prepared via an AAO-assisted template route. *Dalton Trans.* **2014**, *43*, 5713–5720. [CrossRef]
115. Islam, M.; Srivastava, A.K.; Basavaraja, B.M.; Sharma, A. "Nano-on-Micro" approach enables synthesis of ZnO nano-cactus for gas sensing applications. *Sens. Int.* **2021**, *2*, 100084. [CrossRef]

116. Imran, M.; Rashid, S.S.A.A.H.; Sabri, Y.; Motta, N.; Tesfamichael, T.; Sonar, P.; Shafiei, M. Template based sintering of $WO_3$ nanoparticles into porous tungsten oxide nanofibers for acetone sensing applications. *J. Mater. Chem. C* **2019**, *7*, 2961–2970. [CrossRef]
117. Zhang, L.; Tian, J.; Wang, Y.; Wang, T.; Wei, M.; Li, F.; Li, D.; Yang, Y.; Yu, H.; Dong, X. Polyoxometalates electron acceptor-intercalated $In_2O_3$@$SnO_2$ nanofibers for chemiresistive ethanol gas sensors. *Sens. Actuators B Chem.* **2024**, *410*, 135728. [CrossRef]
118. Sun, B.; Liu, M.; Wang, Q.; Song, P. Enhanced formaldehyde gas sensing properties of p-$LaFeO_3$/n-$Fe_2O_3$ composite nanofibers synthesized by electrospinning method. *Sens. Actuators B Chem.* **2025**, *426*, 137010. [CrossRef]
119. Nemufulwi, M.I.; Swart, H.C.; Shingange, K.; Mhlongo, G.H. ZnO/$ZnFe_2O_4$ heterostructure for conductometric acetone gas sensors. *Sens. Actuators B Chem.* **2023**, *377*, 133027. [CrossRef]
120. Shingange, K.; Swart, H.C.; Mhlongo, G.H. Enhanced ethanol sensing abilities of fiber-like $La_{1-x}Ce_xCoO_3$($0 \leq x \leq 0.2$) perovskites based-sensors at low operating temperatures. *Sens. Actuators B Chem.* **2023**, *377*, 133012. [CrossRef]
121. Goto, T.; Hyodo, T.; Ueda, T.; Kamada, K.; Kaneyasu, K.; Shimizu, Y. CO-sensing properties of potentiometric gas sensors using an anion-conducting polymer electrolyte and Au-loaded metal oxide electrodes. *Electrochim. Acta* **2015**, *166*, 232–243. [CrossRef]
122. Mabakachaba, B.M.; Numan, N.; Shingange, K.; Madiba, I.G.; Letsoalo, M.R.; Khumalo, Z.M.; Nkosi, M.; Mhlongo, G.H.; Halindintwali, S.; Maaza, M. Synthesis and $NO_2$ sensing characteristics of Mg-functionalized $VO_2$ (M) Nanorods. *Mater. Sci. Eng. B* **2025**, *318*, 118232. [CrossRef]
123. Song, Z.; Zhou, S.; Qin, Y.; Xia, X.; Sun, Y.; Han, G.; Shu, T.; Hu, L.; Zhang, Q. Flexible and wearable biosensors for monitoring health conditions. *Biosensors* **2023**, *13*, 630. [CrossRef]


**Disclaimer/Publisher's Note:** The statements, opinions and data contained in all publications are solely those of the individual author(s) and contributor(s) and not of MDPI and/or the editor(s). MDPI and/or the editor(s) disclaim responsibility for any injury to people or property resulting from any ideas, methods, instructions or products referred to in the content.